Progress report

Jonas Refsgaard

September 1, 2014

1 Introduction

I have now been a member of the experimental nuclear physics group in Aarhus for one and a half year, and in this report I will describe my work during that period. Since my work is very much motivated by problems in nuclear astrophysics, I start by introducing some of the most basic concepts of nuclear astrophysics. This should hopefully lead to an easier understanding of the following sections containing the more detailed background and motivation for my work. The last part of the report is then dedicated to my own work and the two experiments I have taken part in, the KVI-experiment and the JYFL-experiment.

2 Thermonuclear reactions

Let us have an overview of the mechanisms involved in the thermonuclear reactions that occur in stars. If we consider a simple situation with only two nuclear species, 1 and 2, that can take part in a nuclear reaction, we can write the reaction rate as

$$r = N_1 N_2 v \sigma(v)$$

where N_1 and N_2 are the densities of the two species, v is their relative velocity and $\sigma(v)$ is the reaction cross section. The expression assumes that all the nuclei moves with the same, fixed, relative velocity, but this is of course never true. Rather their velocity is described by a probability distribution, $P(v)$, that satisfies $\int_0^\infty P(v)\,dv = 1$, and from this we find the reaction rate

$$r = N_1 N_2 \int_0^\infty P(v)\sigma(v)v\,dv = N_1 N_2 \langle \sigma v \rangle,$$

where $\langle \sigma v \rangle$ is now the reaction rate per particle pair.

We now consider only stellar environments where the particles are non-relativistic, non-degenerate and in thermodynamic equilibrium. In other words, the nuclei behave as a gas and this means that their velocity distributions are Maxwellian. The relative velocities between the nuclear species are then also described with a Maxwell-Boltzmann distribution, that is

$$P(v) = 4\pi\left(\frac{m}{2\pi kT}\right)^{\frac{3}{2}} v^2 \exp\left(-\frac{mv^2}{2kT}\right),$$

where $m = m_1 m_2/(m_1 + m_2)$ is the reduced mass of the particles. With this knowledge we can write the reaction rate per particle pair as

$$\begin{aligned}\langle \sigma v \rangle &= 4\pi\left(\frac{m}{2\pi kT}\right)^{\frac{3}{2}} \int_0^\infty \sigma(v) v^3 \exp\left(-\frac{mv^2}{2kT}\right) dv \\ &= \left(\frac{8}{\pi m}\right)^{\frac{1}{2}} \frac{1}{(kT)^{\frac{3}{2}}} \int_0^\infty \sigma(E) E \exp\left(-\frac{E}{kT}\right) dE. \end{aligned} \tag{1}$$

In this result we have also substituted v for the center of mass energy $E = mv^2/2$. Our expression for $\langle \sigma v \rangle$ now explicitly takes the thermal velocity distribution into account, but there is more physics still hidden in $\sigma(E)$, particularly we will now investigate the properties of charged particle reactions a bit further.

Consider two positively charged ions at a distance r to each other. The interaction potential $V(r)$ is sketched in Figure 1, and it consists of two parts: A Coulomb-repulsion that dominates at large r and the

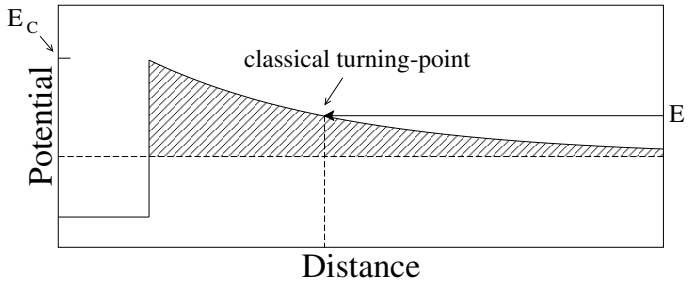

Figure 1: *A sketch of the Coulomb barrier that the charged particle has to tunnel through in order for a reaction to occur. The reaction rate depends strongly on the height of this barrier.*

attraction by the strong nuclear force that dominates at small r. If the center of mass energy E of the two ions is smaller than the maximum value of the potential E_C, then there is a classical turning-point beyond which they cannot approach each other any further and nuclear interactions will be impossible. This barrier is called the *Coulomb-barrier*, and naïvely we would expect nuclear reactions to occur only at temperatures where a significant fraction of the ions have kinetic energies larger than E_C. From quantum mechanics, however, we know that it is possible for a particle to tunnel through a potential barrier, and this effect actually turns out to allow nuclear reactions already at much lower temperatures where $kT \ll E_C$.

Obviously, the probability for the ions to penetrate the Coulomb-barrier must go into the reaction cross section. At low energies ($E \ll E_C$) this penetration probability can be approximated with the so-called *Gamow-factor*, such that

$$\sigma(E) \propto \exp(-2\pi\eta)$$

where $\eta = Z_1 Z_2 e^2/(4\pi\epsilon_0 \hbar v)$ is known as the *Sommerfeld-parameter* and proportional to $E^{-\frac{1}{2}}$.

Another factor we need to take into account is the "size" of the ion. In a very simple interpretation we can imagine the ion as a sphere with a radius equal to the de Broglie wavelength, $\lambda\!\!\!^{-}$. The sphere would then have a geometrical cross section $\pi\lambda\!\!\!^{-2} \propto E^{-1}$, and we incorporate this energy dependence into our reaction cross section by writing

$$\sigma(E) = \frac{1}{E}\exp(-2\pi\eta)S(E), \tag{2}$$

where we have introduced the *astrophysical S-factor*, $S(E)$, which now incorporates all the interesting nuclear physics.

To summarize, we have factorised the cross section for thermonuclear reactions into a part that is related to the de Broglie-wavelength, a part that is related to the Coulomb-interaction, and the astrophysical S-factor, $S(E)$. One motivation for doing so is the fact that $\sigma(E)$ may vary by many orders of magnitude over the range of astrophysically interesting energies while $S(E)$ can be almost constant or at least slowly varying over the same range of energies. we will see in a minute why this property is useful.

With the cross section in the form of (2) , let us rewrite our expression for the reaction rate per pair from (1).

$$\langle\sigma v\rangle = \left(\frac{8}{\pi m}\right)^{\frac{1}{2}} \frac{1}{(kT)^{\frac{3}{2}}} \int_0^\infty S(E)\exp\left(-\frac{E}{kT}\right)\exp(-2\pi\eta)\,dE.$$

If we assume $S(E) \sim$ const. we can move the S-factor outside the integral and the integrand becomes $\exp(-E/(kT))\exp(-2\pi\eta)$. For a fixed temperature the product of these two exponentials is a function only of energy and describes an asymmetric peak called the *Gamow-peak*, see Figure 2. The main contribution to the reaction rate comes from this peak, and the peak position, E_0 can be calculated from

$$E_0 = \left[\left(\frac{\pi}{\hbar}\right)^2\left(\frac{Z_1 Z_2 e^2}{4\pi\epsilon_0}\right)^2\left(\frac{m}{2}\right)(kT)^2\right]^{\frac{1}{3}}.$$

As sketched in Figure 2, E_0 is usually much higher than kT, and if we take the particular example of the $^{12}C(\alpha,\gamma)^{16}O$-reaction which occurs during quiescent He-burning in stars at $T \sim 0.1\,\mathrm{GK}$, we get $E_0 \sim 300\,\mathrm{keV}$ while $kT \sim 10\,\mathrm{keV}$.

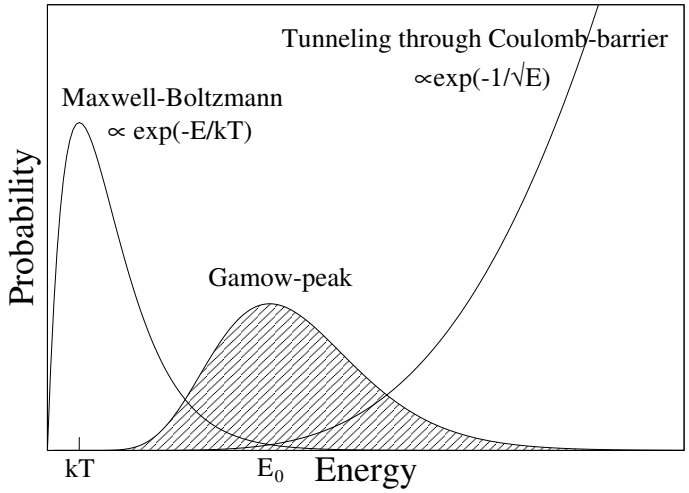

Figure 2: *The energy of the ions follow a Maxwell-Boltzmann distribution. Only the most energetic ions have a good chance of penetrating the Coulomb-barrier, which means that nuclear reactions mainly take place where the two probability distributions overlap, in the Gamow-peak.*

The existence of the Gamow-peak (also called the Gamow-*window*) means that it is of particular importance to know the behaviour of the cross section at and around the peak energy if we want to determine the reaction rates in stellar environments. Unfortunately this energy range is normally too low to be accessible through nuclear experiments, and the cross sections are only known through extrapolation from measurements done at higher energies. Now, this is where the astrophysical S-factor comes in handy! As already mentioned, cross sections can vary very rapidly, and especially at low energies it is difficult to do robust extrapolation of the cross section. The S-factor, on the other hand, has no extreme variations and it is more often the S-factor that is extrapolated from higher energies, and from this the cross section can be obtained for energies in the Gamow-window.

What has been described in this section is the *non-resonant* contribution to the nuclear reaction rate. Non-resonant reactions are one-step processes and one example could be a direct proton- or α-capture where the charged particle is captured and a γ-ray is emitted "in the same go". Now, we will turn to another type of reactions that also contributes significantly to the production of elements in stars.

2.1 Resonant reactions

Resonant reactions proceed through the formation of an intermediate *compound nucleus* and are essentially two-step processes. The scheme is illustrated in Figure 3. This compound nucleus is also called a resonance

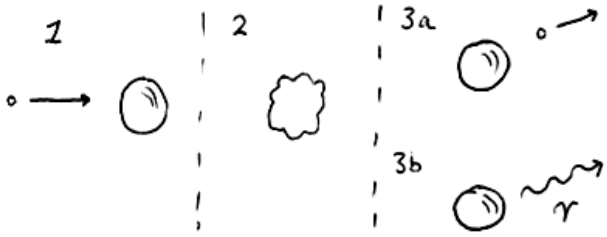

Figure 3: *A projectile hits a target and a compound nucleus (a resonance) is formed (1). The compound nucleus is now highly excited, which is illustrated by its deformed shape (2). Since the system is unbound it can get rid of the excitation energy by particle emmision (3a), but it can also relax by γ-emission (3b) and form a stable nucleus.*

and it is an unbound state which has a wavefunction that inside the range of the nuclear potential is very similar to the wavefunction of a bound state. In the remainder of this section we will consider α-capture

followed by γ-emission, but this is only one example of a radiative capture-reaction. For the cross section of such a reaction we can formally write

$$\sigma \propto \left|\left\langle \mathrm{B}\left|H_\gamma\right|\mathrm{B}^*\right\rangle\right|^2 \left|\left\langle \mathrm{B}^*\left|H_\alpha\right|\mathrm{A}+\alpha\right\rangle\right|^2 = \Gamma_\gamma\Gamma_\alpha,$$

where H_α takes both nuclear and Coulomb interactions into account, B^* represents the resonance and H_γ is the electromagnetic interaction responsible for γ-emission. Furthermore we have introduced the *partial widths*, Γ_γ and Γ_α.

If a resonance exists at the center of mass energy of the projectile and target, E, it may show up as a peak in the cross section described by the *Breit-Wigner* line shape

$$\sigma(E) \propto \frac{\Gamma_\gamma\Gamma_\alpha}{(E-E_R)^2+(\Gamma/2)^2}. \tag{3}$$

Here E_R is the resonance energy measured from the $\mathrm{A}+\alpha$ threshold and $\Gamma = \Gamma_\gamma + \Gamma_\alpha$ is the total width of the resonance. Resonances come in two flavours: The narrow resonances where the width is much smaller than the resonance energy ($\Gamma \ll E_R$), and the broad resonances where the width is a significant fraction of the resonance energy. If the resonance is narrow it is usually permissible to ignore the energy dependence of the partial widths when integrating (1) to get the reaction rate, but in general the widths are functions of energy.

When substituting (3) into (1) we see that it is the overlap between the Maxwellian energy-distribution and the resonance peak that determines the reaction rate. If we consider a narrow resonance, reactions essentially only occur at the resonance energy, and integration gives us

$$\langle\sigma v\rangle \propto \frac{\Gamma_\gamma\Gamma_\alpha}{\Gamma}\exp\left(-\frac{E_R}{kT}\right). \tag{4}$$

In a way we can then, if the resonance is narrow, consider the resonance peak to *be* the Gamow-peak. A narrow resonance can be of particular importance if it occurs at low energy, i.e. a resonance located

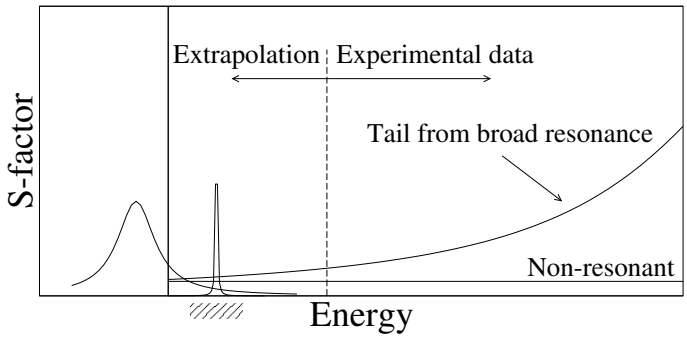

Figure 4: *An overview of the different contributions to the reaction rate or, equivalently, to the astrophysical S-factor. The hatched area marks the Gamow-window. There is a sub-threshold resonance with a tail that extends into the Gamow-window, there is a narrow resonance in the middle of the Gamow-window and then there is a tail contribution from a broad resonance at high energy. All this is on top af the non-resonant contribution.*

just above the particle threshold. Here the Boltzmann factor, $\exp(-E_R/(kT))$, enhances the contribution from the resonance exponentially as E_R approaches kT, and the resonant contribution to the reaction rate quickly becomes dominating. Narrow resonances near threshold play an important rôle in the 3α-process that produces ^{12}C.

Reactions can also proceed through broad resonances. Since these are often located at high energies ($E_R \gtrsim 1\,\mathrm{MeV}$) it is only the part of the resonance which "tails" down into the Gamow-window that contribute to the reaction, see Figure 4. As mentioned in the previous section it is often impossible to measure cross sections at energies in the Gamow-window, so most of the time we perform experiments at higher energies to determine the properties of resonances. To be able to extrapolate the resonance tail down to the Gamow-window we need a detailed understanding of the partial widths' behaviour as functions of energy. For the particle channels we achieve this by introducing the *reduced width*, γ^2, such that

$$\Gamma_l(E) = 2\gamma^2 P_l(E, R_n), \tag{5}$$

where $P_l(E, R_n)$ is the *penetration factor* which includes the probability of penetrating both the Coulomb barrier and the centrifugal barrier. With the centrifugal barrier determined by $V_{\rm cf}(r) = l(l+1)\hbar^2/(2mr^2)$ and the nuclear radius, R_n, the penetration factor is naturally dependent both on the orbital angular momentum, l, and on R_n. A somewhat involved treatment results in $P_l(E, R_n) = (F_l^2(E, R_n) + G_l^2(E, R_n))^{-1}$, where F_l and G_l are the regular and irregular Coulomb functions[1]. This procedure is analogue to the procedure from earlier when we found the penetration probability through only the Coulomb barrier to be proportional to $\exp(-2\pi\eta)$, and indeed we have $P_0(E, R_n) = \exp(-2\pi\eta)$ which makes perfect sense, since the centrifugal barrier is absent for $l = 0$. The situation is a bit different for the γ-decay channel, where the partial width behaves as

$$\Gamma_L(E_\gamma) = \alpha_L E_\gamma^{2L+1} \tag{6}$$

where L is the multipolarity of the emitted γ-photon. Extrapolation of the resonant contribution to astrophysical energies is now straightforward since we know the energy-dependence of the partial widths. The interpretation of the S-factor is no longer very clear since the penetrability is now incorporated in the partial widths, but we can actually define it in a sort of "backward" way by inverting (2), so

$$S(E) = E\exp(2\pi\eta)\sigma(E),$$

which will still mostly reflect nuclear physics properties.

One complication that we have to consider, is the effect of interference between two broad resonances or between a resonance and the non-resonant background. If there are multiple broad resonances that can contribute to a reaction, we have to sum the contributions from each to get the total reaction rate. If two overlapping resonances even have the same spin and parity (J^π) we have to sum the contributions coherently which opens up for quantum mechanical interference effects and these can both be constructive and destructive. When interference occurs in the Gamow-window it is necessary to know the parameters of the involved resonances very accurately in order to calculate a realistic reaction rate.

Finally, imagine a nucleus with an excited state just below the particle-threshold. This state will always have the possibility to γ-decay to a lower state or the ground state, and this means that it must have a finite width in energy. As a result the particle-channel opens up beacuse the state now has a tail which extends up to energies above the particle-threshold, and this tail makes particle capture through the subthreshold state possible. When this happens we are dealing with a *subthreshold resonance*, and these can also play significant parts in capture-reactions, most notably in the ^{12}C$(\alpha,\gamma)^{16}$O-reaction.

3 He-burning in stars

The main part of the life of a star is spent on the main sequence where quiescent H-burning in the core supplies the star with energy. When the hydrogen fuel in the core is exhausted, the star is left at the end of the main sequence with a core consisting mainly of the ashes from the H-burning, helium, and the H-burning continues in a surrounding shell, depositing even more helium in the core. Slowly the core contracts and as a result the temperature and density rise until the point where helium ignites and the production of heavier elements begins. The temperature in the He-burning regions of the star is typically around 0.1 GK to 0.2 GK and the star is now in the *red giant* phase of its evolution. We are particularly interested in the production of ^{12}C and ^{16}O and in the following sections we will take a look at the two involved processes, namely the $(3\alpha,\gamma)^{12}$C-reaction (normally just called the triple-alpha-process) and the ^{12}C$(\alpha,\gamma)^{16}$O-reaction.

3.1 The triple-alpha process

After the idea that all heavy elements were synthesised in stars had been accepted, the question of how the so-called mass gaps at $A = 5$ and $A = 8$ (meaning that no stable isotopes exist with these mass numbers) where bridged, remained open for some time. Since we observe a lot of ^{12}C in the universe there must be a way to effectively combine the α-particles that are the ashes of H-burning to produce ^{12}C. The first step could be the reaction between two α-particles which would have ^{8}Be as its product, but since ^{8}Be is an unbound nucleus with the ground state 92.1 keV above the $\alpha + \alpha$-threshold, the newly formed ^{8}Be would immediately break up again with a lifetime of $\sim 1 \times 10^{-16}$ s.

How about a reaction where three α-particles collide and produce ^{12}C directly? Well, although this is energetically possible, the probability for three α's to be at the same place at the same time is negligible, so we have to come up with some other idea. As it turns out, the ground state in ^{8}Be acts as a narrow

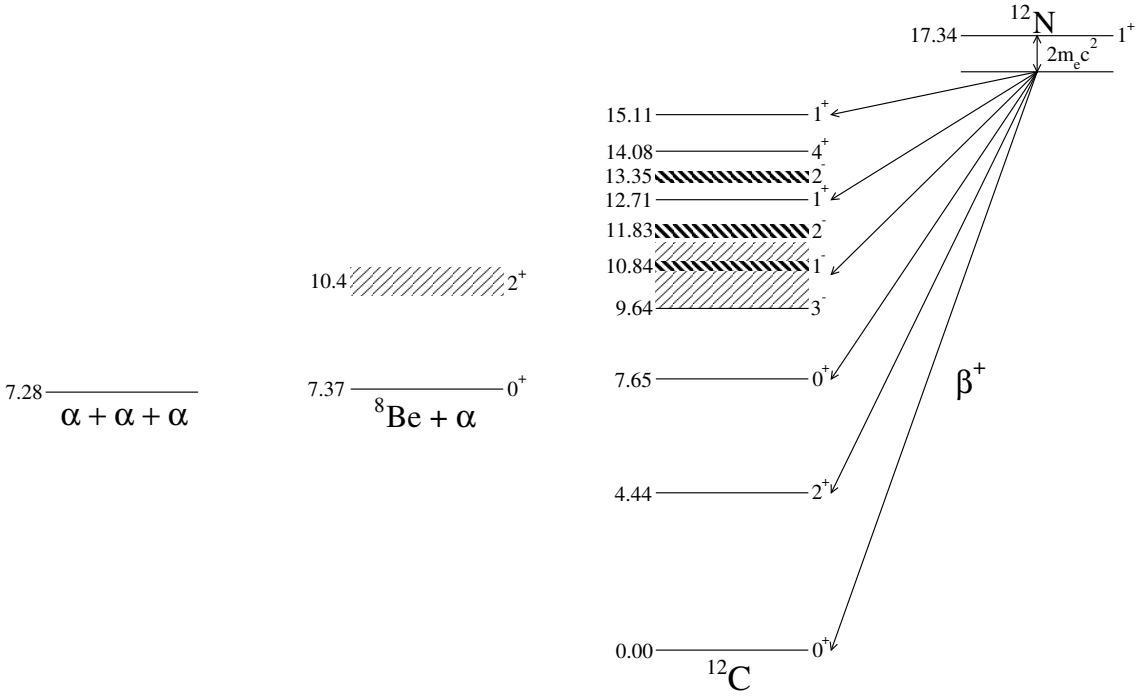

Figure 5: *A diagram with relevant levels for the triple-alpha process. The data are taken from the compilation [2] which is now somewhat dated, but we can nevertheless get a general overview of the level structure. The lightly hatched region represents the very broad resonance structure that is observed which may be the result of several overlapping resonances. It is this region that we are particularly interested in.*

resonance for reactions between two α's and for $T \sim 0.1$ GK it is placed right in the middle of the Gamow-window, thus enhancing the reaction rate enormously. This means that we achieve an equilibrium for $\alpha + \alpha \rightleftarrows {}^8\mathrm{Be}$ where the concentration of ^{8}Be is actually significant ($N(^8\mathrm{Be})/N(^4\mathrm{He}) = 5.2 \times 10^{-10}$[1]). Now the $^8\mathrm{Be}(\alpha,\gamma)^{12}\mathrm{C}$-reaction must do the remaining job and finally we got our ^{12}C produced.

When these ideas came up in the early 1950s there were no known excited states in ^{12}C near the $^8\mathrm{Be}+\alpha$ threshold that could act as a resonance for the $^8\mathrm{Be}(\alpha,\gamma)^{12}\mathrm{C}$-reaction, but the astrophysicist Fred Hoyle showed in 1953 that a non-resonant contribution to the reaction rate could not alone explain the observed abundance of ^{12}C in the universe. This fact led Hoyle to predict that there should also be a resonant contribution, and he even used the observed elemental abundance ratio ^{4}He:^{12}C:^{16}O to calculate its energy to be 7.68 MeV, or 310 keV above the 3α-threshold[3]. Later that year a state was found experimentally at the predicted energy[4], and Hoyle's prediction has since been regarded as one of the most remarkable successes of astrophysics. As a note of historical interest I would like to point out that some experimental evidence for what would later become known as the *Hoyle-state* actually already existed before 1953, but the early observations were not conclusive[5, 6].

3.2 Production of oxygen

With a way to produce ^{12}C, the stellar nucleosynthesis proceeds with the production of heavier elements. The next step on the ladder is ^{16}O which is the product of α-capture on ^{12}C, a reaction that has a signifiant rate already at 0.1 GK. As a result the 3α- and $^{12}\mathrm{C}(\alpha,\gamma)^{16}\mathrm{O}$-reactions take place simultaneously, and the relative universal abundance of the two elements is determined exclusively by the ratio between the reaction rates at stellar He-burning temperatures. For the $^{12}\mathrm{C}(\alpha,\gamma)^{16}\mathrm{O}$-reaction the Gamow-peak is at approximately 300 keV and the cross section at this energy therefore determines the reaction rate.

Several of the mechanisms discussed in sections 2 and 2.1 play important rôles for the reaction: There is a non-resonant contribution which because of fundamental isospin selection rules gives only the possibility of E2-capture to the ground state. There are also multiple resonances through which α-capture can take place, as is seen on the level diagram in Figure 6, and for instance the 2^+-resonance at $E = 6.92$ MeV (corresponding to a resonance energy of $E_R = -245$ keV) is a good example of a subthreshold state acting

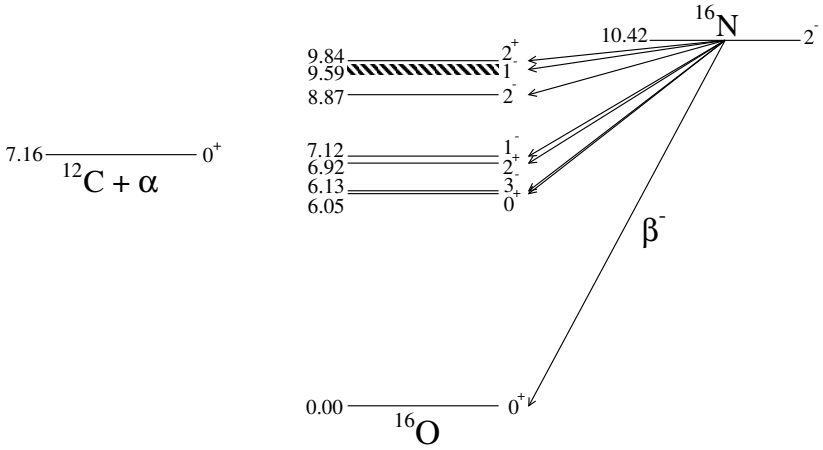

Figure 6: *Levels relevant for the* $^{12}\mathrm{C}(\alpha,\gamma)^{16}\mathrm{O}$*-reaction. Also, the level of the* $^{16}\mathrm{N}$ *ground state is shown to indicate the idea behind the KVI-experiment. All data is from the compilation [7].*

as a resonance. Since a capture through the high-energy tail of the 2^+-resonance also involves an E2-transition, we cannot distinguish this reaction from the non-resonant capture, and the two contributions must be added coherently which, as discussed earlier, means that interference effects will show up, either constructive or destructive. There are two more states that can act as resonances, namely the 1^--states at 7.12 MeV and 9.59 MeV ($E_R = -45$ keV and $E_R = 2418$ keV, respectively). Again, since the spin-parity are 1^- for both states, α-capture through any of them involves an E1-transition and there will be interference between the two contributions. The entire situation is sketched in Figure 7.

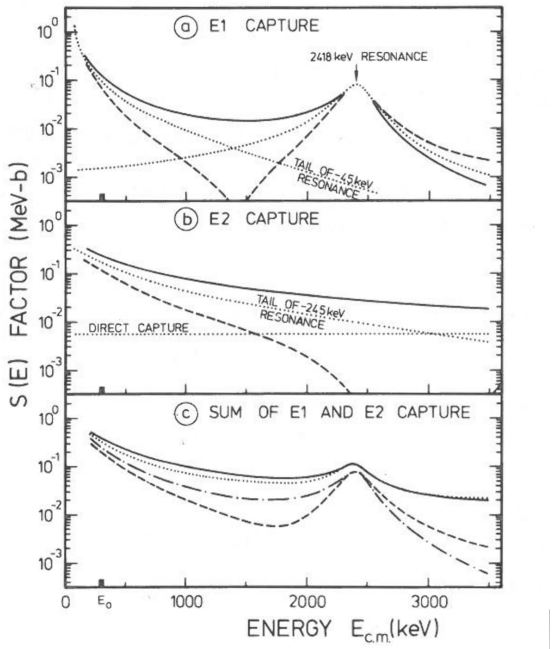

Figure 7: *A sketch of the two contributions to the* $^{12}\mathrm{C}(\alpha,\gamma)^{16}\mathrm{O}$*-reaction and the important effect of interference between different reaction channels. The contributions to the S-factor from individual resonances and the non-resonant capture are shown with dotted lines in (a) and (b) for E1- and E2-capture, respectively. The resulting S-factor is also shown with constructive (solid line) and destructive (dashed line) interference terms taken into account. In (c) we see the total S-factor for each of the four interference-schemes. The figure is reproduced from [1].*

It is worth noting that although there are several resonances for the $^{12}\mathrm{C}(\alpha,\gamma)^{16}\mathrm{O}$-reaction, none of them

are positioned inside the Gamow-window and hence they only contribute through their relatively weak tails and the reaction rate is limited. This fact has profound consequences for the observed elemental abundances, because if a resonance had appeared in the Gamow-window, as is the case for the $2\alpha \rightarrow {}^{8}$Be- and ${}^{8}\mathrm{Be}(\alpha,\gamma){}^{12}$C-reactions, the reaction rate would have been greatly enhanced. In this way the ^{12}C produced in the 3α-proces would have been almost depleted at the end of stellar He-burning and carbon-based life as we know it would not have existed.

4 The nuclear physics cases

We have now covered most of the fundamentals and also seen some hints of the astrophysical significance of the nuclear properties of ^{12}C and ^{16}O. It is now time to take the plunge and look at the nuclear physics motivation for the two experiments I have taken part in.

4.1 Excitations of the Hoyle-state

Because of the importance of the Hoyle-state in ^{12}C-synthesis it has naturally been the subject of much attention since its existence was established in 1953. Already in 1956, Hirohito Morinaga noted that the self-conjugate nuclei ^{8}Be, ^{12}C, ^{16}O, ^{20}Ne and ^{24}Mg all had low-lying 0^+-states accompanied by a 2^+-state not too far above[8]. Morinaga showed that this structure could be explained by considering the low-lying 0^+-states to be highly deformed (i.e. non-spherical) nuclei with large moments of inertia, and the 2^+-states would then be rotational excitations of the deformed states. In ^{16}O and in ^{24}Mg the spacing between the levels even seemed to fit with the moment of intertia of a chain-like structure with four and six, respectively, α-particles in a line, and it was suggested that the Hoyle-state could fit in this scheme as a chain of three α-particles. If this was indeed the case, the Hoyle-state had to have spin-parity 0^+ and there had to exist a 2^+-state at around 9.7 MeV excitation energy. After the spin and parity of the Hoyle-state had been established experimentally to be 0^+ and after some resonance strength with $E_R = 10.1(2)$ MeV and $\Gamma \approx 2.5$ MeV that could be either 0^+ or 2^+ had been seen[9, 10], Morinaga reiterated his hypothesis and argued that the broad resonance had to be 2^+, which would agree with it being interpretated as a rotational excitation of the Hoyle-state[11]. Although this picture may seem appealing, it is probably oversimplified. That the ^{12}C-nucleus has a high degree of α-clustering is beyond doubt, though, and we shall later hear about several experimental results that supports this fact.

An alternative interpretation of the resonance strength around 10 MeV was put forth in 1962[12], where the broad resonance-like structure in the spectrum was explained as the *ghost* of the Hoyle-state. Now, a ghost is a peak in the spectrum that is not a real resonance, but rather associated with a lower-lying state near the particle-threshold. The cross-section from this level is described by the Breit-Wigner line shape from (3), and this cross section can actually produce two peaks if, in some energy range, the numerator grows faster than the denominator as function of increasing energy. In other words, if the penetrability grows faster than the high-energy tail of the Lorentzian falls off. It was estimated that the Hoyle-state, which is a level near the particle-threshold, would give rise to a ghost peak at around 9.2 MeV with a FWHM of approximately 5 MeV, and the ghost was thought to be able to account for all the observed strength in this energy range. Later experiments involving β-decay spectroscopy of both ^{12}B and ^{12}N produced spectra that were not well fitted with the ghost as the only contribution[13], but instead needed two broad, resonant contributions on top of the ghost.

The last theoretical model of the ^{12}C-nucleus that we shall describe, is a model that assumes $\mathcal{D}_{3h}$-symmetry of the ^{12}C ground state[14]. This is just a fancy and non-intuitive way of saying that the ^{12}C ground state is an equilateral triangle with an α-particle at each vertex, and in this respect it is also one of the cluster-models. With this as the starting point all other (cluster-like) excitations are considered to be rotational and vibrational excitations of the triangular system, and the energy levels can be calculated as

$$E = E_0 + Av_1 + Bv_2 + CL(L+1) + D(K \pm 2l)^2. \tag{7}$$

where v_1 and v_2 are the vibrational quantum numbers for a breathing mode and a bending mode vibration, respectively, L is the angular momentum, K is the projection of angular momentum onto a body-fixed axis and l is somehow the angular momentum of the bending mode vibration. The result is the energy level diagram in Figure 8 where each rotational band is labelled by the vibrational quantum numbers (v_1, v_2^l). The levels in the $(0, 0^0)$ rotational band are rotations of the ground state and the levels in the $(1, 0^0)$-band are rotations of the Hoyle-state. Very recently some experimental evidence supporting the triangle-model

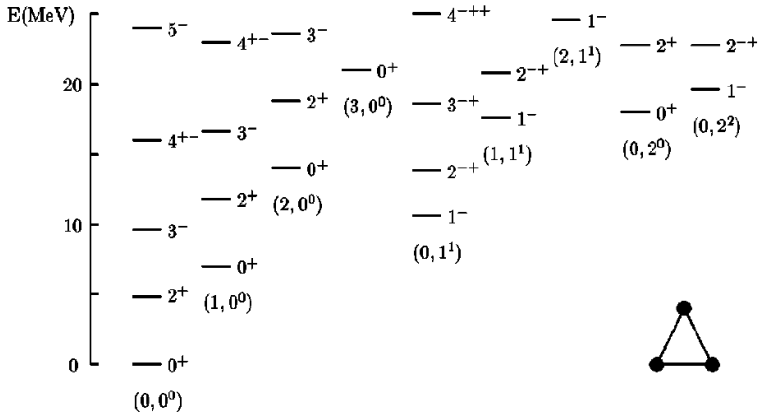

Figure 8: *The figure shows the energy levels of the ro-vibrational excitations, calculated with (7). The numbers in the parantheses indicate the quantum numbers (v_1, v_2^l) of each rotational band. It should be noted that the level spacing are the same in all bands, which is the result of the formula not taking the moment of inertia's dependence on the vibrational excitation into account. Reproduced from [14].*

appeared, because the 5^--state that it predicted at the top of the ground state band, was observed in inelastic scattering experiment with 40 MeV α-particles scattering of a ^{12}C-target[15]. In the same paper the triangle model are revisited, and the fact that the moments of inertia are dependent on the level of vibrational excitation is now taken into account. As a result the Hoyle-band now have a smaller level spacing or, equivalently, a larger moment of inertia. This is sensible from the point of view that the Hoyle-state itself should be a breathing mode vibrational excitation of the ground state with the excitation resulting in the triangle becoming more extended. For now, let us just note that the triangle-model, if we accept it as a good model, provides us with quite detailed predictions of which states we should expect to appear in ^{12}C.

In the last decade numerous experiments experiments have been performed with the purpose of improving our understanding of the broad resonances in ^{12}C. In a β-decay study of ^{12}N and ^{12}B[16] a common analysis was done for experiments parformed at the IGISOL-facility in Jyväskylä (see section 6) with segmented detectors and full kinematical information on the 3α-breakup, and at KVI in Groningen (see section 5), which showed that the experimental data could be fitted with two broad states, respectively a 0^+ and a 2^+, with $E_{0^+} = 11.2(3)$ MeV, $\Gamma_{0^+} = 1.5(6)$ MeV, $E_{2^+} = 11.1(3)$ MeV and $\Gamma_{2^+} = 1.4(4)$ MeV, and an additional state above the 12.7 MeV-resonance with either 0^+ or 2^+. Another analysis of data from inelastic p- and α-scattering on ^{12}C[17] seems to indicate a narrower 2^+-resonance at somewhat lower energy, namely at $E_{2^+} = 9.75(15)$ MeV with a width of $\Gamma_{2^+} = 0.750(150)$ MeV, and finally a ^{12}C$(\gamma, 3\alpha)$-experiment[18, 19] shows a 2^+-state with $E_{2^+} = 10.03(11)$ MeV and $\Gamma_{2^+} = 0.80(13)$ MeV. If it is the same state that is measured in the three experiments then clearly the results are not compatible.

In conclusion, the situation regarding the character of the broad resonances above the Hoyle-state is still quite confusing. It seems clear, though, that the region is dominated by 0^+-strength and that there must be some 2^+-strength buried somewhere underneath. Whether or not it can be regarded as a rotational excitation of the Hoyle-state is also a question open for interpretation. Further experiments are required which are able to give a good handle on the spin and parity of the observed states in order to distinguish the different contributions, and in that way hopefully help clarifying the situation.

4.2 Determining the ^{12}C$(\alpha,\gamma)^{16}$O reaction rate

As already mentioned in section 3.2 there are many states and effects that contribute significantly to the ^{12}C$(\alpha,\gamma)^{16}$O-reaction. Direct measurement of the cross section is not feasible because of its rather small value for energies in the Gamow-window, $\sigma(300\,\text{keV}) \sim 1 \times 10^{-17}$ b, so the only option is to measure at higher energies and extrapolate down to $E_0 = 300$ keV. Measurements exist for energies down to approx. 1 MeV, but to be able to do a reliable extrapolation the α-widths of the involved states must be known with good accuracy[20]. One way to get information on these is to study the β-delayed α-spectrum from the

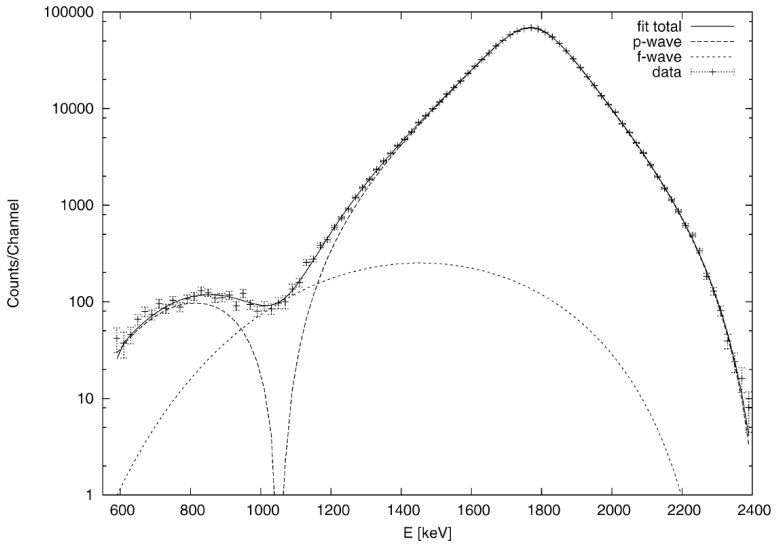

Figure 9: *A high-statistics measurement of the β-delayed α-spectrum from ^{16}N, performed at TRIUMF[21]. On top of the data points is an R-matrix fit and the dashed lines show that both p-wave and f-wave components are needed to fit the data. The horizontal axis displays the α-particle energy. Reproduced from [20].*

decay of ^{16}N (you can see the decay scheme in Figure 6) and do an *R*-matrix fit[1] to extract the α-widths, at least for the states relevant for $E1$-capture, and a lot of work has been done along these lines. Most of the important experiments are reviewed in [22], and it seems that the state of the art spectrum has been produced by a group at TRIUMF[21], see Figure 9. Since the E1 cross section at 300 keV is dominated by the subthreshold 1^--resonance at 7.12 MeV, the α-width of this state is a very important parameter to determine. As should be clear from Figure 7(a), there is interference between the 7.12 MeV-state and the 9.6 MeV-state, and this shows up in the β-delayed α-spectrum in Figure 9 as a deformation of the tails of the broad peak with 2.4 MeV breakup energy (corresponding to an α-particle energy of 1.8 MeV). A scenario with constructive interference is currently favoured, but that is still a matter of discussion. In other words, the shape of the tails, most notably the low-energy tail, of this α-peak is quite sensitive to the properties of the subthreshold 7.12 MeV-state, and that is why the spectrum is useful for determination of the α-width of this state.

From [21] the recommended value for the astrophysical S-factor is $S_{E1}(E_0) = 79(21)$ keV b, but it is also clear from [22] that the β-delayed α-spectrum of ^{16}N has been the subject of considerable controversy in the last 20 years, and some authors even claim that a value for the S-factor as low as $S_{E1}(E_0) = 10$ keV b is consistent with the known data[23]. Therefore it would be desirable to constrict some of the parameters that go into the *R*-matrix fit, for instance the branching ratio for the β-decay of ^{16}N to the broad 9.6 MeV 1^--state in ^{16}O. The current value for this branching ratio was found in the early 1970s to be $1.13(8) \times 10^{-5}$, but a more precise determination would help reduce the error on $S_{E1}(E_0)$ significantly[22, 24].

5 The KVI-experiment

The purpose of this experiment (officially named P20) is to measure the branching ratio for the β-decay of ^{16}N to the 9.6 MeV-state in ^{16}O. A collaboration of scientists from Aarhus University and KU Leuven went to the *Kernfysisch Versneller Instituut* (KVI) in Groningen, the Netherlands, to do the experimental work at the AGOR/Triμp facility which consists of the AGOR cyclotron and the Triμp magnetic separator[25]. Here a radioactive beam of ^{16}N with an energy of $\sim$ 60 MeV/ion were produced in inverse kinematics by leading the primary beam of ^{15}N with energy 105 MeV/ion through a gas cell 10 cm long containing CD_2 gas at 1.2 atmospheres, producing ^{16}N in a (d, p)-reaction. Most of the primary beam and various beam contaminants like other isotopes or different charge states of ^{16}N were removed in the magnetic separator

[1] The *R*-matrix formalism is just a way of describing the properties of a nuclear state with parameters like the energy, spin, parity, total width and partial widths.

and in the end it was a quite pure ($\sim$ 60 %) beam of ^{16}N that entered our target chamber. The beam was implanted in an active stopper and it is now our job to count (1): The number of implanted ^{16}N-ions and (2): The number of α-decays from the 9.6 MeV-state in ^{16}O. Since the statistical uncertainty goes as $1/\sqrt{N}$ we need to observe at least 2500 decays to achive 2 % accuracy.

5.1 Experimental setup

Several detectors were employed in the experimental setup, a sketch of which is shown in Figure 10: The ΔE-detector is an unsegmented Si-detector with a thickness of 60 µm and part of a socalled *telescope* setup with the DSSSD, furthermore acting to slow down the beam such that it doesn't punch through the DSSSD. The DSSSD-detector seen in Figure 11 is described in detail in [26]. It is a highly segmented Si strip-detector with dimensions 16 mm×16 mm×78 µm. With 48 300 µm wide strips on both front(p) and back(n) side it has a total of 2304 pixels, each representing an active volume of approximately 300 µm × 300 µm × 78 µm silicon. The advantage of a detection volume this small is that the β-particles, which always comes

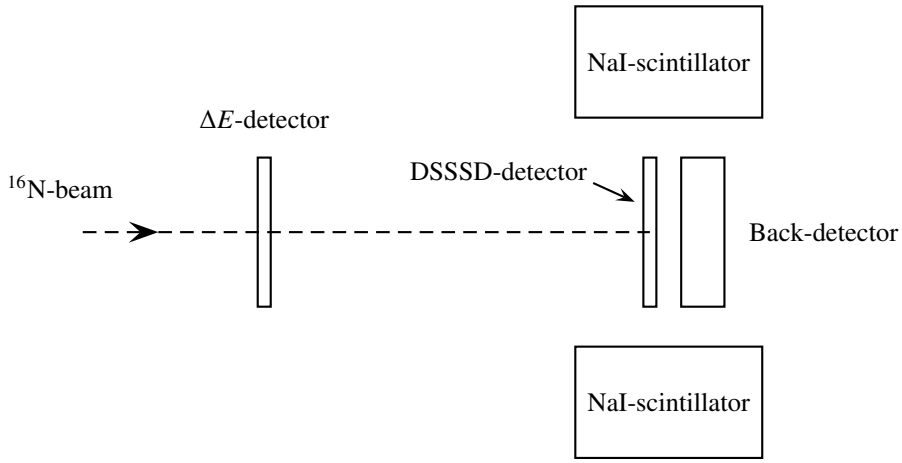

Figure 10: *A sketch of the experimental setup (not to scale). Details on the different detector can be found in the text.*

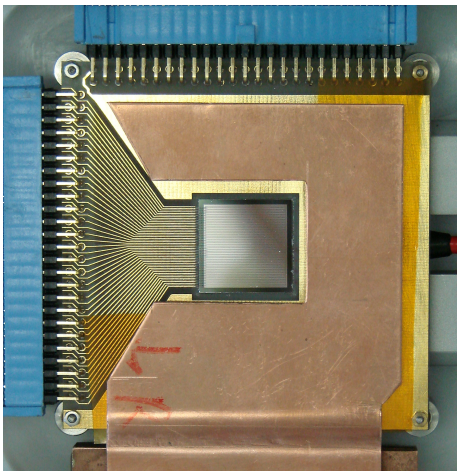

Figure 11: *A picture showing the DSSSD-detector. The copper surrounding is a part of the liquid cooling system.*

in coincidence with the α-particles of interest, doesn't get the chance to deposit a significant part of their energy in the pixel before leaving it. This is both an advantage when we have to distinguish between β- and α-particles and also the effect of β-summing is minimised. The final Si-detector is the socalled back-detector which is 300 µm thick and unsegmented. All these detectors were placed in a vacuum chamber at

$\sim 10^{-6}$ torr and two NaI-scintillators were placed outside the chamber. The trigger was an OR between the DSSSD-, the ΔE- and the NaI-detector.

The idea is now to let the ^{16}N-ions in the beam pass through the ΔE-detector and deposit some of their energy in this detector. With the right choice of beam energy and detector thickness the ions should now have just enough energy to pass half-way through the DSSSD-detector and stop. By measuring the energy loss in the ΔE-detector and the remaining energy that is deposited in the DSSSD we can make a $\Delta E - E$ plot and each ion species in the beam will show up in different loci ("blobs") in the plot, thus enabling us to use the $\Delta E - E$ plot for particle identification. This is useful since the beam will never be completely pure, and it will also allow us to discriminate between beam-triggered events and decay-triggered events because we should see a signal in the ΔE-detector for all beam-triggered events. On the other hand an event with a signal in the DSSSD and no signal in the ΔE-detector must be a decay-event. The Back-detector was placed in close geometry with the DSSSD in order to catch the β-particles going "straight" out of the DSSSD. In principle the DSSSD-spectrum from these events should be a slightly cleaner α-spectrum since the β-particles leaving the DSSSD orthogonally to the detector plane are those depositing the least amount of energy in the DSSSD. The two scintillators were used during the experiment to confirm that it was indeed ^{16}N that was implanted in our detectors. Looking for the characteristic γ-lines in ^{16}O is far quicker and more robust way of identifying the ^{16}N than waiting for a PhD-student to produce a $\Delta E - E$ plot with properly calibrated energies. With a good efficiency calibration the scintillators can also provide an independent estimate of the total number of implanted ^{16}N-ions.

Each implanted ^{16}N-ion deposited 30 MeV to 36 MeV in the DSSSD but with the dynamic range extending to these energies it would not be possible to get a high-resolution α-particle spectrum in the range around 2.4 MeV. In order to circumvent this challenge two independent amplifier chains were used for the DSSSD, with the low-gain chain having a dynamic range of 80 MeV and the high-gain chain having a dynamic range of 8 MeV. This allows us to use the signal in the low-gain channels for particle identification in implantation events and the signal in the high-gain channels to get a good spectrum from the decay-events.

5.2 Course of events

The original plan was to run with continuous beam for the entire experiment and use the ΔE-detektor to identify beam-events and decay-events. A calibration with an external calibration source containing the three α-emitters ^{239}Np, ^{241}Am and ^{244}Cm was to be complemented with an internal calibration done with implantation of ^{20}Na which also emits α-particles with well-known energies. The plans changed slightly during the experiments, and in Table 1 you can find an overview of the most important events. If the reader feels confused by the fact that most gains were changed between the ^{16}N-runs and the internal calibration with ^{20}Na, the explanation is that the heavier ^{20}Na-ions simply deposits more energy, around 120 MeV, and this was outside the dynamic range with the old amplifier settings. In that way the ^{20}Na-calibration almost defied its purpose, and in the clarity of hindsight it would probably have been smarter to add a thicker degrader foil before the detectors, in order to reduce the beam energy.

5.3 Calibration of the DSSSD

I have already shown a picture, Figure 11, of the DSSSD that was used in this experiment. To familiarise the reader with this kind of detector we will take a short introduction to the basic principles. DSSSD stands for *double sided silicon strip detector*, and it is basically a silicon wafer, doped to act as a diode-detector, where the charge-collecting contacts are segmented into thin strips running along orthogonal directions on the front side and the back side, as sketched on Figure 12. Normally the detector would be operated with a reverse bias voltage sufficient to deplete the free charge carriers (electrons and holes) in the entire silicon wafer, so the silicon effectively makes up the *active layer* of the DSSSD. When an energetic charged particle travel through the active volume, it gradually loses its energy by forming electron-hole pairs in the silicon until it either comes to rest or leaves the detector again. The free charges are then swept out of the active volume and collected on the metal contacts on both sides, and since the collection electrodes are segmented, the detector is actually position sensitive. One of the drawbacks of the design is that the aluminium contacts and the oxide insulation on the surfaces acts as *dead layers* through which the charged particles must pass before reaching the active volume, and this in turn means that some of the energy of the particle is deposited in the dead layers and thus is not detected. Energy loss in the dead layers is one of the big challenges when working with precision energy spectroscopy, and the effect must be carefully taken into account when the detector is calibrated.

Table 1: *A short overview of the most important events during the KVI-experiment. The experiment was done during May 2013.*

Date	*Description*
13th	Our beam time starts and by the end of the day the beam has been guided through the separator to our setup. For now we are running in continuous mode
14th	Because it hadn't been possible to extract a clean decay spectrum from the data, we switched in the late evening to a pulsed beam, i.e. 15 s beam on followed by 15 s beam off in cycles.
15th	A logic signal was fed from the beam chopper to our acquisition such that it is possible to distinguish whether an event occurred during beam on or beam off. Finally it was possible to see the α-particles from the decay of ^{16}N and the experiments was left in this state until there was a break in the beam time of a few days, due to Pentecost.
18-20th	During Pentecost a 24 h calibration run with the external α-source was done.
21st	The facility was restarted and by mid afternoon we again had the ^{16}N-beam directed to the target chamber.
22nd	To be able to detect a larger portion of the decays we switched to a cycle with 1 s beam on and 7 s beam off.
23rd	End of the ^{16}N-beam. The cyclotron team was asked to produce a ^{20}Na-beam instead and meanwhile the gains of both DSSSD-chains were changed.(!)
24th	Several unfortunate circumstances hampered the experiment and it was not until the late afternoon we got useful data with ^{20}Na. The rest of the time we were running with 0.5 s beam on and 1 s beam off.
25th	End of experiment. After some short calibration runs with the external α-source and a ^{60}Co γ-source we packed up and went home.

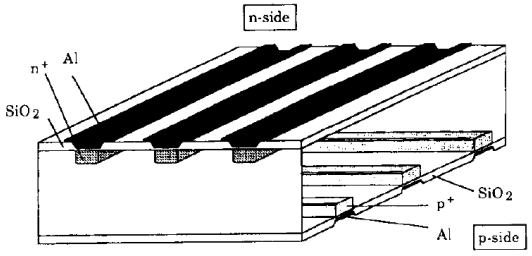

Figure 12: *This figure shows the basic principles behind the construction of a DSSSD. It is seen how the active layer of silicon is sandwiched between layers of aluminium contacts and insulating oxide. Reproduced from [27].*

External calibration

To calibrate the detector, we used, as already mentioned, an external source with three α-emitters whose α-energies are listed in Table 2. A typical spectrum from a calibration is seen in Figure 14a, and we will

Table 2: *A list of reference α-energies and intensities for the α-emitters that was used for calibration of the DSSSD. It should be noted that with typical energy resolutions $\sim 25\,\text{keV}$ it is not possible to distinguish the two ^{239}Pu-peaks with the highest energies, and one must use the weighted mean ($5148.89\,\text{keV}$) as calibration energy. The values are those recommended by [28].*

Isotope	I_α [%]	E_α [keV]
^{239}Pu	73.3	5156.59
	15.1	5144.3
	11.5	5105.8
^{241}Am	85.1	5485.56
	13.3	5442.80
^{244}Cm	76.4	5804.77
	23.6	5762.16

have a brief look at how such a spectrum is produced and some of its general features: When a particle hits the detector it will produce a signal in one of the front strips and one of the back strips and trigger an event in the data acquisition (the DAQ). If noise is present in some of the channels it will also be recorded. In the analysis of a calibration run one defines a threshold at, say, channel 1000 (for common ADCs with 12 bit resolution there are 4096 chanels in total), and for each event ignores all signals smaller than this threshold. Furthermore, if there is exactly one of the front strips and one of the back strips with any signal larger than the threshold, it is assumed that they belong to the same physical particle, and that the particle hit the detector at the intersection between the two strips. One ends up with a spectrum similar to Figure 14a for each of the front and back strips, and the task is now to determine the positions of the three main α-peaks and correlate it with the α-energy, to get a calibration for the channels.

The calibration spectrum in Figure 14a is dominated by the three primary α-peaks. For ^{241}Am and ^{244}Cm the two secondary α-peaks are also clearly distinguishable and for ^{239}Pu we can see the tertiary α-peak. Also readily visible on the plot are the low-energy tails of the α-peaks which extends down to zero energy. This tail is a consequence of the nature of the energy deposition of charged particles in solids, and the entire peak-shape is described by a socalled Landau-distribution. This makes determination of the peak position a little flaky, since the Landau-distribution has no mathematically defined mean, and the method most suitable depend somewhat on the amount of counting statistics available. One way could be to fit the peak with a Gaussian peak folded with an exponential tail on the low-energy side, and then use the mean of the Gaussian as the peak position. In this work I have used a peak finding algorithm based on a numerical deconvolution of the spectrum with a Gaussian function[29] which arguably does not return a value with a very well-defined meaning, but it is very robust and stable, even with low statistics spectra.

The energies in Table 2 are raw α-energies, but since the source is sealed, and because the DSSSD has a dead layer thickness of 339(3) nm Si-equivalent, we must bear in mind that the α-particles have lost some of their energy before entering the active volume. The energy loss in the detector dead layer with thickness d can be estimated as

$$\Delta E = d\frac{dE}{dx}(E = 5.5\,\text{MeV}),$$

and since $dE/dx(E = 5.5\,\text{MeV}) = 1350\,\text{MeV cm}^{-1}$ for silicon [30], we get $\Delta E = 45\,\text{keV}$. This loss is only for particles travelling straight through the dead layer, and it would be larger if the particle was to travel through the dead layer with an angle to the normal of the detector surface, see the sketch in Figure 13. It is possible to use this effect to determine the dead layer thickness by looking at the position dependence of the detector signal. If the source is placed centrally in front of the detector, and not too far away, then for each strip the signal will be smaller near the edge of the detector and largest near the middle. Looking at the situation in Figure 13, if a particle is emitted with an angle θ to the axis its path through the dead layer will be extended by a factor $1/\cos(\theta)$, and the energy loss will go as $\Delta E(\theta) = \Delta E(\theta = 0)/\cos(\theta)$. The maximum effect is found at the edge where $\theta = \arcsin(l/(2D))$, and for our case, where $D = 5\,\text{cm}$ and $l = 1.6\,\text{cm}$, it

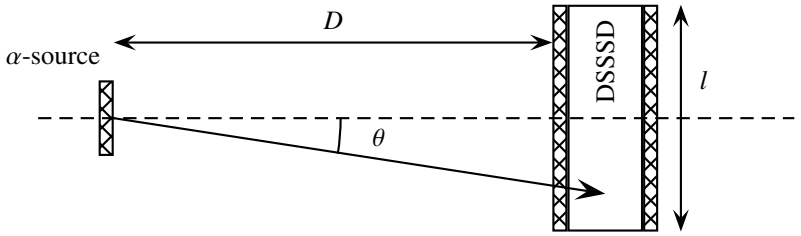

Figure 13: *An α-particle hitting the DSSSD near its edge needs to travel a longer distance through the dead layer (hatched area) before reaching the active volume of the detector.*

amounts to a variation in the energy loss of 0.6 keV, or roughly one quarter of an ADC-channel, which is much too small to be of any use in the determination of the dead layer thickness of our detector with the amount of counting statistics in our calibration runs.

I had not done these simple estimates before I looked for the effect in the data because in that case I would probably never have spent the effort, but to my surprise there seemed to be a mechanism with the exact opposite effect. The signal was *smaller* in the center of the DSSSD than at the edges, which is illustrated in Figure 14. I divided each strip into three sections and filled individual spectra for each section.

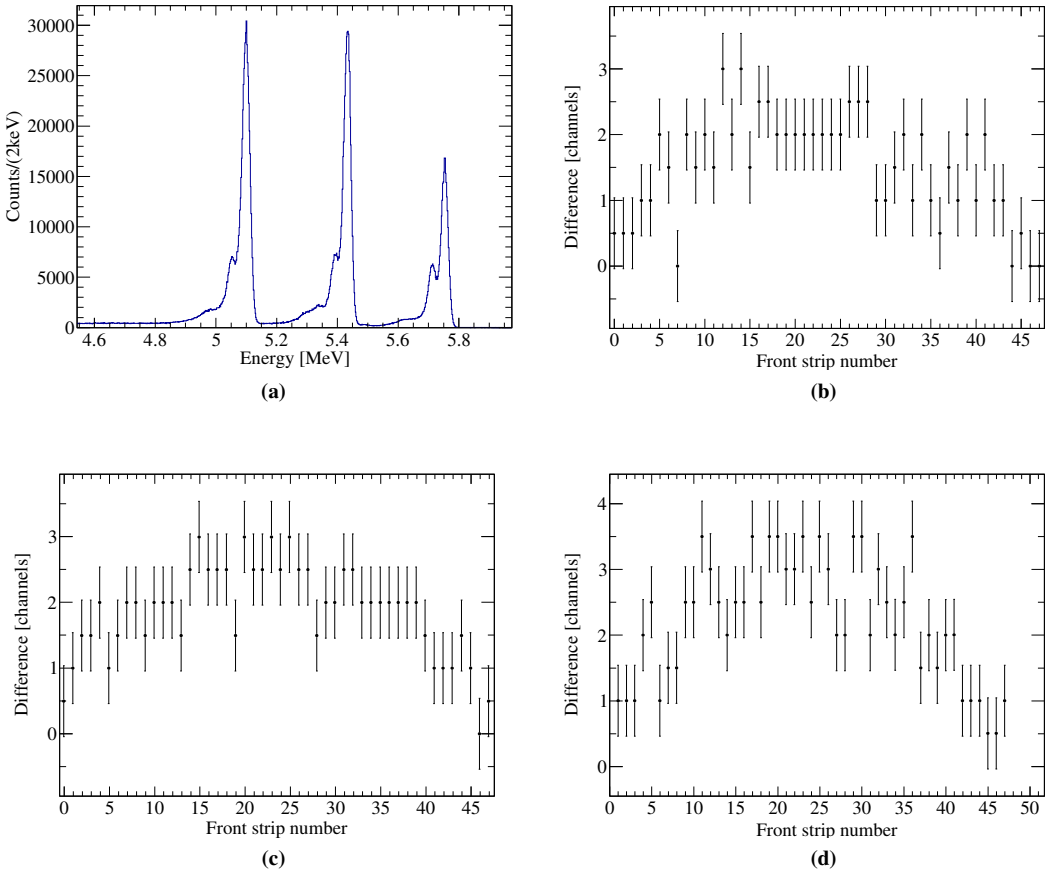

Figure 14: *In (a) we see the calibration spectrum from the entire DSSSD for the longest calibration run during the KVI-experiment, taken during Pentecost. The plots in (b), (c) and (d) are explained in the text.*

For each spectrum I found the position of the three primary α-peaks and for each peak subtracted the peak position in the middle section from the mean peak position of the two outer sections. The results are shown in Figure 14b, 14c and 14d for the ^{239}Pu-, ^{241}241- and the ^{244}244-peaks, respectively. It is clear that there is a systematically smaller response in the middle of the DSSSD than at the edge, and it even seems to

be an energy dependent phenomenon, since the typical response difference is around two channels for the ^{239}Pu-peak while it is closer to three channels for the ^{244}Cm-peak. Because the effect is significant, with a response difference of three channels corresponding to roughly 5 keV, I naturally sought for its possible origin.

External effects One possible explanation could be that the dead layer thickness of the detector is not uniform, and that the maximum thickness is in the middle of the detector. It is not uncommon to see this kind of variation, although it normally occurs on larger detectors.

Internal effects If the concentration of impurities in the semiconductor material was significantly larger in the center of the detector than at the edge, it could explain why the signal is smaller in the center. The reason would be that impurities (or defects) can trap the free charge carriers and act as recombination centers, and in that way less charge would be collected by the surface electrodes.

One way to distinguish between the two effects would be to look for the same effect in the internal calibration with implanted ^{20}Na because if it was a dead layer effect it would not affect the response to internally emitted α-particles. On the other hand, if the effect was caused by impurities in the semiconductor it would appear for the internal αs also. In the end my analysis was hampered by poor statistics and no conclusion was reached through analysis of the data. I believe that the matter is settled now, though, through personal communication with Professor Phil Woods from the University of Edinburgh, who is one of the designers behind the DSSSD we used. It turns out that it is completely normal to see a degradation of the charge pulse shape of the detector as it is being used for implantation experiments. For every single implantation you basically introduce an impurity to the semiconductor crystal and this kind of detector does in general not have a very long service life. As the leakage current also went up monotonously during the KVI-experiment, also indicating a rising concentration of impurities, I think that many arrows now point in the direction of an internal effect.

Internal calibration

The internal calibration was done by implanting ^{20}Na in the detector at the end of the experiment. This isotope emits α-particles with very well-measured energies and should provide a calibration free of annoying dead layer effects. A direct calibration of the ^{16}N data is not possible because, as has already been

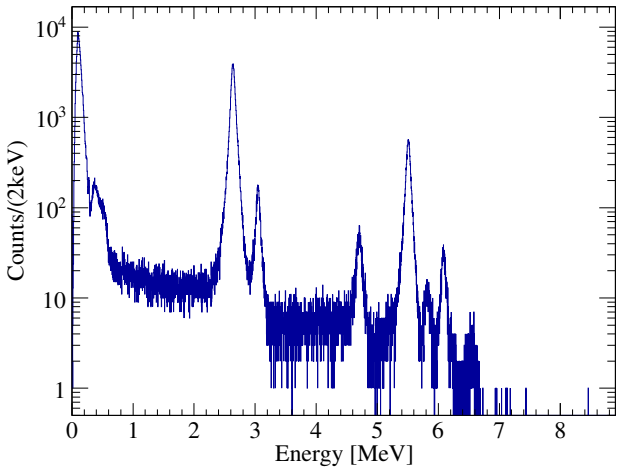

Figure 15: *A DSSSD spectrum produced from the entire* ^{20}Na *data set. The two highest peaks are used for internal calibration.*

mentioned, the gains of all the amplifiers were adjusted in the break when the beam was changed from ^{16}N to ^{20}Na. A short ($\sim$ 1 h) run was done with the external α-source on the last day of the experiment, i.e. with the same amplifier settings as during the ^{20}Na-runs, and this has made it possible for me to compare the two types of calibrations. Since I know the expected energy loss of the α-particles in the detector dead layer, I know their initial energies from Table 2, and I know the energy they deposit in the active volume of

the detector (using the internal calibration from ^{20}Na), it is possible to calculate any residual energy losses that the α-particles may have suffered. These losses are expected because the α-emitters are deposited on the source in a layer with a finite thickness, and some sources are even covered by an extra layer of sealing. When the residual losses have been determined, I can use the result to correct the external calibration of the ^{16}N-data and hopefully produce an accurate energy spectrum.

The ^{20}Na decay spectrum is seen in Figure 15 and I have used the two most prominent peaks for the calibration. These peaks correspond to excitation energies in ^{20}Ne of 7422 keV and 10 273 keV (2692 keV and 5543 keV above the ^{16}O + α threshold, respectively), and the obvious procedure would be to calibrate to these energies. However, there are three effects involved that we must consider, if we want to use this calibration for detection of α-particles: Firstly, the ^{20}Na decay is a β-delayed α decay, so the α-breakup is always preceded by the emission of a β-particle, which of course also deposits some of its energy in the detector (an effect known as β-summing). Secondly, the emission of the β-particle results in a recoil of the remaining ^{20}Ne-nucleus and this energy is deposited in the detector. Lastly, in the breakup into ^{16}O and an α-particle, due to energy and momentum conservation, one fifth of the breakup energy goes to the ^{16}O-nucleus and four fifths to the α-particle. When the ^{16}O-ion deposits its energy in the detector, the energy is not converted as efficiently to electron-hole pairs as it happens for an α-particle, so if the data is calibrated with a standard α-source, the observed breakup energy of ^{20}Ne is 66(4) keV smaller than the released energy. Numbers obtained by GEANT4 simulations are given in Table 3 and a detailed discussion can be found in [31].

Table 3: *Below E is the excitation energy of the relevant level in ^{20}Ne, E_R is the energy above threshold (taken to be 4729.84 keV), E_β is the energy shift of the peaks caused by β-summing, E_{rec} is the β-emission recoil energy, E_{dep} is the total energy deposited in the detector for each decay and E_{obs} is the observed energy if the data are calibrated with data from an α-source. The values are from [32, 31] and are given in* keV

E	E_R	E_β	E_{rec}	E_{dep}	E_{obs}
7421.9(12)	2692.1(12)	26(2)	0.5	2719(2)	2653(5)
10 273.2(19)	5543.4(19)	31(2)	0.2	5575(3)	5509(5)

I have focused my attention on the peak at 5509 keV peak beacause it sits in the middle of the range of energies covered by the external source and therefore in the range where the external calibration is most reliable. By applying the external calibration with tabulated values to the ^{20}Na-data I find the peak position to be 5560(1) keV, which is 51 keV higher than it should be. This means that the energy loss of the α-particles from the external source must have experienced an energy loss of 51(5) keV before entering the active volume of the detector, and this is a loss 6 keV higher than the loss of 45 keV that we calculated for a 5.5 MeV α-particle travelling through the detector dead layer only. This extra loss can be explained if the α-source is covered by a layer of 45(35) nm of Si-equivalent, with the main contribution to the uncertainty coming from the values in Table 3.

5.4 Measuring the branching ratio

Now, it is time to look at the ^{16}N-implantation data. To extract a value for the branching ratio of decay to the 1^--state at 9.6 MeV in ^{16}O we need to identify and count (1) all ^{16}N-implantations in the DSSSD and (2) the number of breakups of the 9.6 MeV-state into ^{12}C + α. When the implantations and decays have been counted there are some corrections that must be applied, for instance due to dead time of the data acquisition or the fact that we are only looking for decays during the periods where the beam is off. In other words we need to *normalise* the data.

Particle identification

The original plan for the experiment was to run with a continuous beam and distinguish between beam-triggered events and decay-triggered events by looking for a signal in the ΔE-detector. It was not, however, possible for us to extract a clean decay spectrum from the continuous beam data, and one probable explanation could be presence of light particles, like protons or deuterons, in the beam. These particles could pass the ΔE-detector without depositing very much energy, in fact the deposited energy could be below the

ADC-threshold, and the particle would go on and be implanted in the DSSSD or punch through it, either way resulting in a signal in the DSSSD which could mimic a decay-event. Whatever the real explanation is we switched to pulsed mode, or *beam on/beam off*, after approximately one and a half day of beam time.

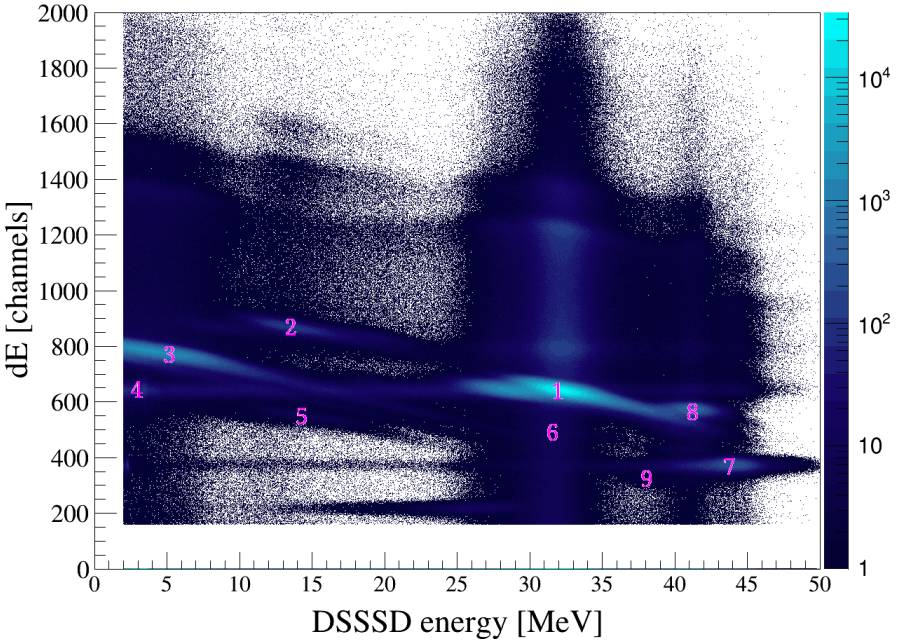

Figure 16: *A plot showing the signals in the ΔE- and the DSSSD-detectors during beam on. This kind of plot is a common way of distinguishing different beam components, and our local expert in energy losses, Oliver Kirsebom, has supplied me with the following identification of the particles in the different loci in the plot: (1) $^{16}N^{7+}$, (2) $^{14}N^{6+}$, (3) ^{13}C, (4) protons, (5) $^{12}C^{5+}$, (6) $^{14}C^{6+}$, (7) $^{13}C^{6+}$, (8) $^{15}N^{7+}$ and (9) $^{11}B^{5+}$. Assuming this is correct we find that ^{16}N makes up around 60 % of the particles in the beam.*

To identify ^{16}N-implantations during beam on I have used the $\Delta E - E$-plot shown in Figure 16. From the figure it is clear that there are many components in the beam, but it is also seen that ^{16}N is the dominant component and that it is implanted with an energy of 30 MeV to 36 MeV. One can use the SRIM software tool to show that with this energy most of the ions are stopped half-way through the detector. Anyway, I have defined a polygon encircling the ^{16}N "blob" in the plot and defined each event inside this polygon to be an ^{16}N-implantation. From the (hopefully) normalisable part of the data I find 1.20×10^8 implanted ^{16}N-ions.

Identifying decays are a bit easier, since all events during beam off must be triggered by a decay. The decay spectrum is shown in Figure 17 and to produce the spectrum I have used the DSSSD-signal that came through the high-gain amplifier chain where the dynamic range is an order of magnitude smaller. On the other hand we get a much better resolution, limited to the intrinsic detector resolution of approximately 28 keV FWHM. The spectrum is essentially free of background, and the broad peak at 2.32(2) MeV is the $^{12}C + \alpha$ breakup of the 9.6 MeV-state in ^{16}O that we looking for. The data that went into Figure 17 represents the part of our total data that I believe is normalisable, and there is a total of 1580 observed breakups. The only other feature of the decay spectrum that I would like to point out is the signal that rises from around 600 keV and downwards in energy. This is the β-signal and because I placed a software cut at 500 keV we only see the very few events with large energy deposition. If I had not imposed any restrictions on the energy, we would see the β-signal as a towering peak extending down to the thresholds of the data acquisition because, due to the smallness of the branching ratio to the 9.6 MeV-state, we see 10^5 β-particles for each α breakup. This also explains why a DSSSD with such a small thickness (78 µm) and with such a high degree of segmentation was chosen for the experiment; if the detection volume had been much larger the β-particles would have had a change to deposit more energy, and the α-peak would have been completely buried in the β-signal.

One way to check if my identification of implantations and decays could be to compare the spatial

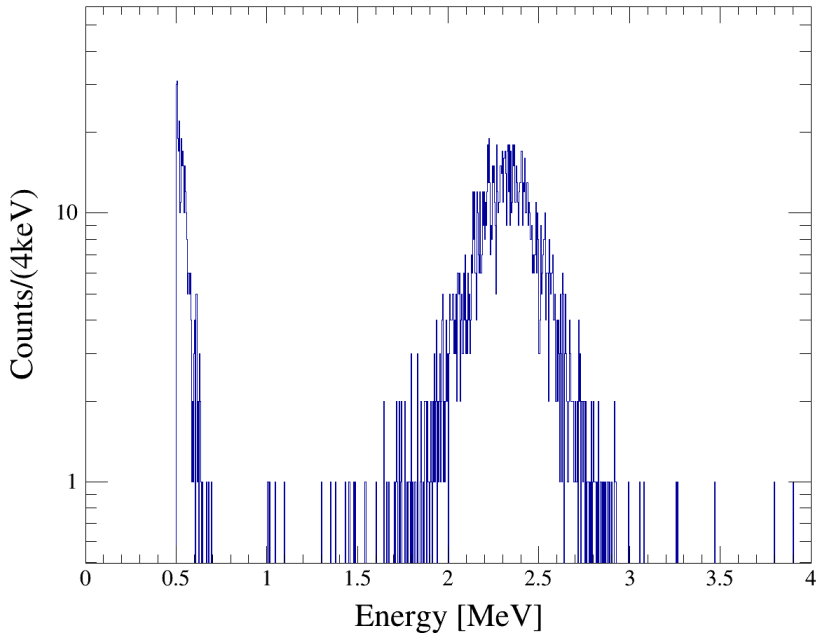

Figure 17: *A decay spectrum showing 1580 observed breakups of the* 9.6 MeV*-state. The spectrum is produced from the DSSSD-signal that went through the high-gain amplifier chain.*

distribution of the events across the DSSSD. The implantation distribution is shown in Figure 18a and the

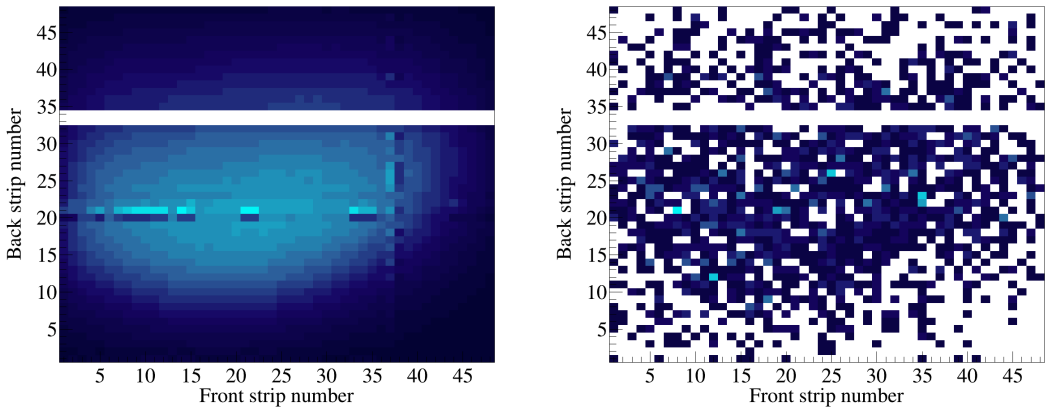

Figure 18: *In (a) we see the implantation pattern on the DSSSD, and in (b) we see the decay pattern. From the figures it is possible to see that back strips number 33 and 34 had broken connections, but since DSSSDs are quite delicate devices it is not uncommon to see a broken strip.*

decay distribution iis shown in Figure 18b. Although I have not done any fancy statistical analysis to show that the two figures represent the same distribution, it doesn't seem very unlikely.

Naïvely one could find the branching ratio by dividing the two numbers we just found, but this would not be correct because of the several effects that must be considered if we want to normalise the data

Correction for pulsed beam

Let us start with the fact that we are only looking for decays during the beam off periods, i.e. only half of the time. Therefore we need to determine the number of decays during beam on time indirectly. Fortunately this number can be obtained by multiplying the number of observed decays by a simple factor, the derivation of which I will briefly sketch in the following: Consider a beam on/off scenario where t_0 is the duration

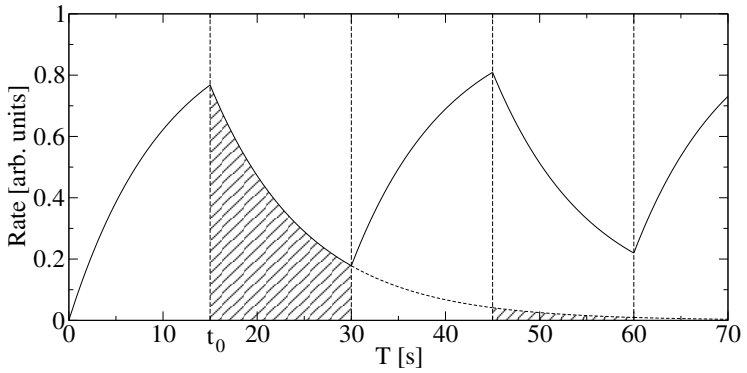

Figure 19: *This plot shows how the decay rate would behave in a beam on/off scenario. The dashed, vertical lines separate the beam on (implantation) periods from the beam off (decay) periods starting from the left with beam on. The solid line shows the total decay rate and the dashed line shows the decay rate of only those ions that were implanted during the first implantation period. The area of the cross-hatched region is the maximum number of those ions that we are able to observe.*

of the beam on period and a is the duration of the entire on/off-cycle in units of t_0. Also, let R denote the implantation rate and λ the decay constant of the implanted ions. In one cycle the number of implanted ions is then $N_I = Rt_0$ and since these must all decay sooner or later, this is also the total number of decays that must result from the implantation. The decay rate at the end of the implantation period is now $R(1 - e^{-\lambda t_0})$ and the ions that remain in the detector decay exponentially with a rate

$$R_{\text{decay}}(t) = R(1 - e^{-\lambda t_0})e^{-\lambda(t-t_0)} = R(e^{\lambda t_0} - 1)e^{-\lambda t}.$$

The number of observed decays, N_O, is the above expression integrated during the following beam off periods, and we can write

$$\begin{aligned}
N_O &= R(e^{\lambda t_0} - 1)\left\{\int_{t_0}^{at_0} e^{-\lambda t}\,dt + \int_{(a+1)t_0}^{2at_0} e^{-\lambda t}\,dt + \int_{(2a+1)t_0}^{3at_0} e^{-\lambda t}\,dt + \cdots\right\} \\
&= R(e^{\lambda t_0} - 1)\left\{\left[-\frac{1}{\lambda}e^{-\lambda t}\right]_{t_0}^{at_0} + \left[-\frac{1}{\lambda}e^{-\lambda t}\right]_{(a+1)t_0}^{2at_0} + \left[-\frac{1}{\lambda}e^{-\lambda t}\right]_{(2a+1)t_0}^{3at_0} + \cdots\right\} \\
&= \frac{R}{\lambda}(e^{\lambda t_0} - 1)\Big\{\left(e^{-\lambda t_0} + e^{-(a+1)\lambda t_0} + e^{-(2a+1)\lambda t_0} + \cdots\right) \\
&\qquad\qquad - \left(e^{-a\lambda t_0} + e^{-2a\lambda t_0} + e^{-3a\lambda t_0} + \cdots\right)\Big\} \\
&= \frac{R}{\lambda}(e^{\lambda t_0} - 1)\Big\{e^{-\lambda t_0}\left(1 + e^{-a\lambda t_0} + e^{-2a\lambda t_0} + \cdots\right) \\
&\qquad\qquad - e^{-a\lambda t_0}\left(1 + e^{-a\lambda t_0} + e^{-2a\lambda t_0} + \cdots\right)\Big\} \\
&= \frac{R}{\lambda}(e^{\lambda t_0} - 1)(e^{-\lambda t_0} - e^{-a\lambda t_0})(1 + e^{-a\lambda t_0} + e^{-2a\lambda t_0} + \cdots).
\end{aligned}$$

We recognise the last paranthesis as a geometric series, and with a, λ and t_0 all being positive the series converges[2] and we get

$$N_O = \frac{R}{\lambda}(e^{\lambda t_0} - 1)\frac{e^{-\lambda t_0} - e^{-a\lambda t_0}}{1 - e^{-a\lambda t_0}}. \tag{8}$$

[2]Convergence of geometric series: $\sum_{n=0}^{\infty} r^n = \frac{1}{1-r} \quad ; r < 1$

With this result it is possible to calculate the ratio between the observed number of decays and the actual number of decays:

$$\frac{N_O}{N_I} = \frac{1}{\lambda t_0}(e^{\lambda t_0} - 1)\frac{e^{-\lambda t_0} - e^{-a\lambda t_0}}{1 - e^{-a\lambda t_0}}. \tag{9}$$

If we take the parameters that are relevant for our experiment, i.e. implantation of ^{16}N for 15 s and a decay period of 15 s, we get a detection "efficiency" of 0.427.

Dead time

When the data acquisition (DAQ) is triggered by a signal, it needs some time to let the ADCs convert the signal and transfer the values from the ADCs to the storage device (a hard drive). During this process the DAQ will not allow itself to be triggered by another signal, and it appears to be "dead", which explains the term *dead time*. Any physical event happening durign the dead time will not be recorded, so we need to know which fraction of the time is dead time to be able to calculate the number of physical events from the number of observed events. One way to get this number is to look at the ratio of the accepted number of triggers to the total number of triggers in some time interval, and in that way you extract the mean detection efficiency during the time interval. When working with this type of analysis I tried to count the number of triggers occuring between the accepted events, and a strange pattern occured, see Figure 20. Normally, for a situation where events are occuring at a certain rate, you would expect this

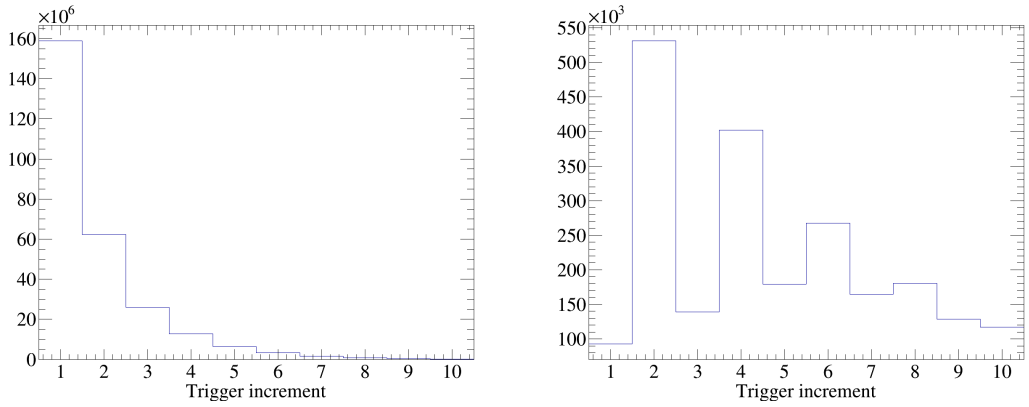

Figure 20: *In these plots we see histograms of how many triggers happened between accepted events in (a) a typical pre-Pentecost run and (b) in a typical post-Pentecost run. For events in the bin labelled* 1 *there were no lost triggers between the preceding event and the current event.*

number to follow a Poisson distribution, like the histogram seen in Figure 20a. For all post-Pentecost runs the histograms look more like Figure 20b, which is certainly not Poissonian. The explanation could be *double triggering*, a phenomenon that can for instance be caused by signal reflections in the cables, due to poor impedance matching, or by ringing of the trigger pulse. A Monte Carlo simulation of a generic trigger looking at a Poisson process and having a certain probability of double triggering reproduces the histogram in Figure 20b nicely, and I am convinced that double triggering has occured during the entire second week of the experiment[3]. Consequently we can not normalise that data by just counting the accepted vs. total triggers, so we need some other method.

Another approach to dead time correction is to try and characterise the dead time of the DAQ in detail by measuring how long it is, i.e. for how many μs the DAQ is dead, and also to figure out if the dead time is *extending* or *non-extending*, and then calculate the actual trigger rate from the rate of accepted triggers[33]. This led me to try and produce histograms of the time interval between events, at first only one-dimensional histograms, but since they didn't really follow any of the expected time interval distributions, so this path was unfruitful. The next idea to test was whether the time interval between any two events showed a

[3] A logbook entry also shows that some of the scaler inputs were changed at the exact time when the double triggering appears.

systematic relation to one of the other observables in our data stream, for instance the "size" of the first of the two events, i.e. how many channels show a signal. The result is shown for the beam on time in

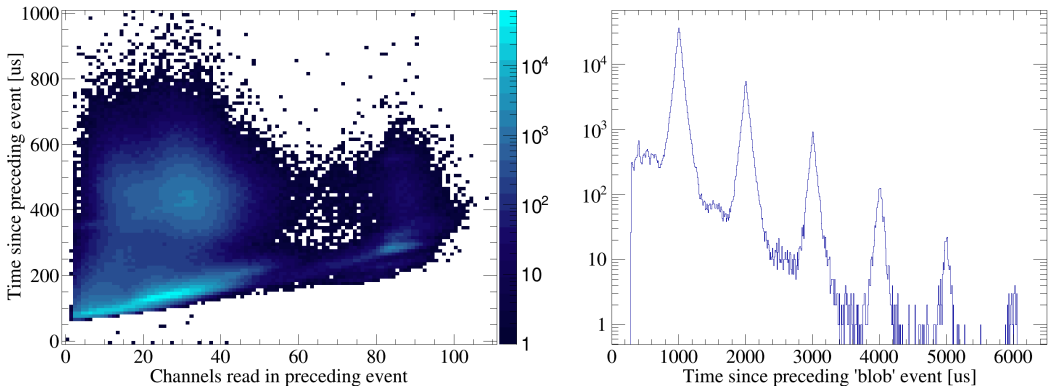

Figure 21: *The histogram in (a) shows the relation between the number of channels that need to be read, converted and stored in a given event, and the time we have to wait before the next event is accepted. The histogram in (b) show the clear periodicity of the strange events in (a) with waiting time larger than* 300 µs.

Figure 21a and there are two things about this histogram that should be noted: Firstly, there is clearly a linear relation between the number of read channels and the time we must wait for the next event, and secondly, there is a collection of some "strange" events where the waiting time is $> 300\,\mu s$, which is significantly longer than for the majority of the events. It was suggested to me that this behaviour could be caused by readout of the ADC buffer, where data from multiple events are stored temporarily before being read out all at once. Even though I knew that our DAQ does not exploit the ADC buffers this suggestion made me look for some periodicity of the strange events with respect to the accumulated amount of data. I didn't see any clear evidence of periodicity until I tried to look for periodicity in time, see Figure 21b, which shows that the strange events occur with a very well defined period of 1 ms. Together with some other evidence this led me to suspect that there had been an intensity modulation of the beam with the beam almost disappearing for $\sim 400\,\mu s$ every 1 ms.

At first I communicated with our contact person at KVI, Hans Wilschut, about the issue. Being a professor in experimental physics at the facility for twenty years he had never heard of such beam modulations, so naturally my perplexity was profuse. However, after direct communication with the cyclotron operators I learned that the beam hed indeed been pulsed with a frequency of 1 kHz, the so-called *duty cycle*, and that adjusting how large a fraction of each ms the beam was one way of manipulating the mean beam current. When the data for Figure 21a was taken the duty cycle had been 72 %, meaning that the beam disappeared for 280 µs every 1 ms, which fits quite well with my initial guess. In fact this is a problem for the dead time correction because we now have different kinds of events occurring in the beam on period with different detection efficiencies. Implantation events of course only happen when the beam is actually on and the trigger rate is very high, but in between the duty-cycle pulses we have only decay- and background-events, triggered by the DSSSD or the scintillators, see Figure 22. The consequence is that we can no longer find the detection efficiency for implantations by simply counting the total triggers and accepted triggers for each 15 s pulse.

Let us estimate the effect of the duty-cycle modulation on the normalisation of implantation events. In the following I use the quantities defined in the caption of Figure 22, and I assume that the background can be described by a constant rate. Since the background also includes decay-events from ^{16}N, which has a half-life of 7.12 s, this assumption is of course not quite true, but for a first order estimate we should be fine. Instead of using n/N as our estimate for the detection efficiency for implantations we must get rid of the events that occurs between the short pulses, i.e. we can calculate the detection efficiency for implantations with the expression $(n - n_b)/(N - N_b)$. Based on the assumption of a constant background and the fact that the beam on and beam off periods are of equal length we get $n_b = n_{\text{off}}(1 - D)$ and $N_b = N_{\text{off}}(1 - D)$. For a specific, but representative, beam on/off cycle from 15th of May we have $n = 31925$, $N = 43924$,

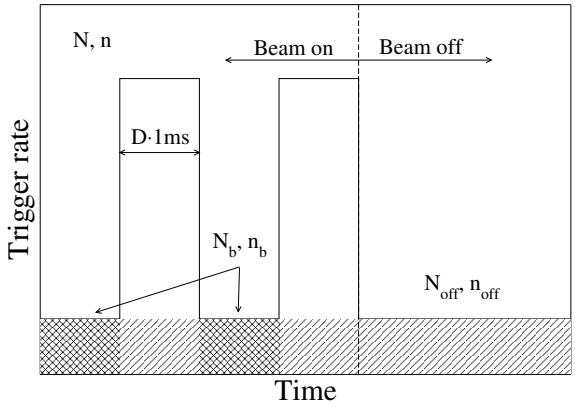

Figure 22: *I have sketched how the trigger rate behaves in a scenario where the beam is pulsed on both very long (*15 s*) and very short (*1 ms*) timescales. N and n are the number of total triggers and accepted triggers, respectively, occuring in the* 15 s *beam on period, while N_{off} and n_{off} denote the same quantities for the following* 15 s *beam off period. N_b and n_b are the total and accepted triggers occurring between the short pulses, respresented by the cross-hatched areas in the figure, and D is the duty-cycle.*

$n_{\text{off}} = 5923$, $N_{\text{off}} = 5996$ and $D = 0.25$, and we can calculate

$$\frac{n}{N} = 0.727 \qquad \text{and} \qquad \frac{n - n_{\text{off}}(1-D)}{N - N_{\text{off}}(1-D)} = 0.697.$$

From these results we can conclude that the naïve estimate of the detection efficiency is off by approximately 3 %, and since the goal of the experiment was to determine a branching ratio with 2 % accuracy it is necessary to take the beam modulation into account.

Charge sharing

As shown on Figure 12 there are insulating layers of SiO_2 between the strips on the surface of the DSSSD. If a charged particle enters the DSSSD through this interstrip region the generated charge signal is shared between the two adjacent strips, but not necessarily with full charge recovery or sometimes even with a negative polarity signal induced in one of the strips[34]. Our detector has strips that are 300 µm wide with an interstrip region of 35 µm, so from pure geometric considerations around 20 % of the implantations must hit the DSSSD in the interstrip regions, and this is supported by the data. My preliminary analysis shows that full charge recovery is possible for the vast majority of the implantations, but there are also events where some charge is lost, and this will disturb the paricle idenfication. Also, it is not clear how the charge sharing behaves when we are looking at decays of the implanted ions, since in a decay none of the electron-hole pairs are generated near the surface. If the probability of charge recovery is equal for implantations and decays it would not disturb analysis, bot if there is a difference we would get a biased result for the branching ratio.

To get a profound understanding of the charge sharing in our DSSSD would require either a very good theoretical model or, even better, sending it to a raster scan facility where a µm-beam can be scanned with high precision across the surface of the DSSSD while the signals are monitored. In conclusion, I think some attention still needs to be directed towards this issue.

5.5 Summary and preliminary results

The fact that we started running with continuous beam for one and a half day before changing to beam on/off combined with the appearance of double triggering means that it will probably only be possible to normalise the data produced between the 15th and the 18th of May, i.e. a little less than three days out of a total of six days of ^{16}N beam time. I have produced the decay spectrum in Figure 17 with the normalisable data, and in total I have found 1580 α-breakups in my analysis. Since the statistical uncertainty is $1/\sqrt{N}$ we get 2.5 % uncertainty from our limited statistics, which is already larger than the 2 % accuracy promised in the proposal. On top of this comes systematic effects, of which I have already mentioned dead time and charge sharing. The rather high beam currents means that during beam on our trigger rate was correspondingly

high, resulting in the DAQ only recording approximately two thirds of the events, which in turn means that the dead time correction must be done very carefully. This statement is supported by the fact that even a seemingly unimportant intensity modulation of the beam can result in an error on the branching ratio of a few percent. Using the $\Delta E - E$-method I have identified 120×10^6 ^{16}N-implantations for the same data set, and performing all the various corrections I end up with a value for the branching ratio of 1.66×10^{-5}.

In principle I would not ascribe an uncertainty much larger then 5 % to this number, since the corrections described in the report have been done with considerable care. However, the value is clearly incompatible with the tabulated value of $1.13(8) \times 10^{-5}$, so I suspect that there must still be some major effect which have not been taken into account, or simply a trivial mistake in my analysis. It should be noted, though, that an independent preliminary analysis, performed during the experiment by Oliver Kirsebom, identified numbers of implantations and decays leading to a very similar, high, value for the branching ratio.

6 The JYFL-experiment

The JYFL-experiment (officially I161) was basically a repetition of an earlier experiment, reported in [35, 36], but with a planned improvement in statistics by at least an order of magnitude. This improvement was provided by an upgrade of the facility and also by the use of a setup with many DSSSDs in close geometry, thus increasing the solid angle coverage of the target. The experiment was done in collaboration with people from the University of York and CSIC in Madrid, with Christian Diget from York being the spokesperson.

JYFL is an acronym for the accelerator laboratory of the University of Jyväskylä, which houses two cyclotrons and the IGISOL facility (another acronym meaning *Ion-Guide Isotope Separator On-Line*), and the latest upgrade, IGISOL-4, is described in [37]. The IGISOL technique is reviewed in [38], and I have only sketched the basic principles in Figure 23. A ^{12}C-target was bombarded with a beam of 30 MeV

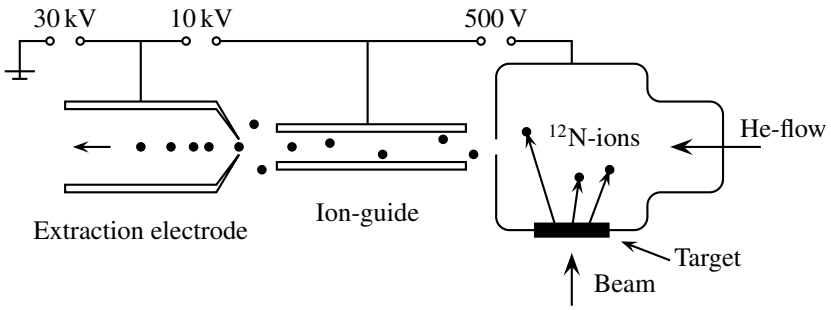

Figure 23: *The principle behind IGISOL. The beam from the cyclotron hits the target and produces the radioactive isotopes. In the reaction some ions recoil out of the target and into a flow of He that sweeps the ions into the sextupole RF ion-guide. The guide separates the isotope of interest and transmits it to the extraction electrode, and after the extraction the isotope-beam is moderately accelerated and directed to the experiment.*

protons from the cyclotron, producing ^{12}N through the ^{12}C$(p,n)^{12}$N-reaction. The ^{12}N-ions were extracted as a low-energy radioactive beam via the IGISOL and directed to our experiment, where the ions were implanted in a thin ($20\,\mu g\,cm^{-2}$) carbon foil. The idea was then to detect the products from the decay, namely the β-particle from the β-decay to ^{12}C and the three α-particles from the following breakup of the populated excited states in ^{12}C, with full kinematic information.

The experimental setup is shown and described in Figure 24. It consisted of nine charged particle detectors in a compact configuration, bringing the solid angle coverage of the target up to around 50 %. The setup allows us to detect all four particles from the β-delayed α-breakup for a significant fraction of the decays, and the use of position-sensitive detectors gives us full information on both energy and momentum of the detected particles. With all the kinematical information it is possible to characterise the excited states in ^{12}C that are breaking up, for instance using the *Dalitz plot*-technique to determine, or at least restrict, the spin-parity of the states that are breaking up.

The experiment was scheduled with three and a half weeks of beam time from June 9th to July 2nd 2014, where the first two weeks would be with ^{12}N-beam, then a few days of ^{20}Na-beam for calibration and the last week we would have a ^{12}B-beam (which also produces excited ^{12}C-nuclei through β-decay, only from the other side of the valley of stability). For all but the ^{20}Na-calibration we would run with beam from

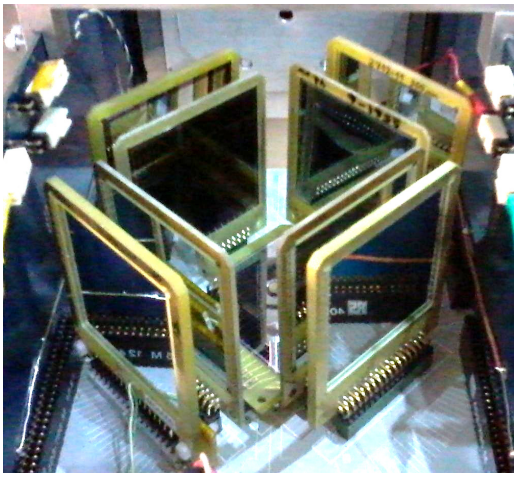

Figure 24: *The detector setup used for the JYFL-experiment. The beam enters the chamber through the small hole seen in the top of the image and the carbon foil was mounted in the middle of the detector "cube" such that the foil was orthogonal to the direction of the beam. The innermost detectors were thin (*$\sim 80\,\mu$m*) DSSSDs for detection of* α*-particles and the outer detectors were thicker (*$\sim 1000\,\mu$m*) Si-detectors, all but one unsegmented, meant for* β*-particle detection. Outside the chamber, approximately* 15 cm *from the target, we had a Ge-detector for detection of the characteristic* γ*-rays from* ^{12}C.

a new cyclotron, the MMC-30 cyclotron, and in the early hours of June 10th the beam tuning was finished and we had identified ^{12}N-decays in our experiment. Alas, four hours later the cyclotron broke down, and the damage was irreparable four the entire duration of the experiment. Eventually some free beam time appeared on the older cyclotron, the K130, and we had ^{12}N-beam from Wednesday 18th till Thursday 26th of June. From preliminary data analysis it seems that the ^{12}N-yield was a little higher than expected, so in the end we have around a factor of 20 more observed 3α-breakups than in the previous experiment from 2004. In Figure 25 I have shown a small part of the data with 3α-events, where the clear diagonal in the upper plot shows that many of the decays proceed through the ^{8}Be ground state, where energy and momentum conservation gives 2/3 of the available energy to one α-particle and the remaining 1/3 is shared between the two other α-particles. The three "blobs" at 5.34 MeV total energy comes from the breakup of the 12.7 MeV-state, which has unnatural spin-parity 1^+, and it is clear that the breakup pattern is different from the surrounding natural spin-parity strength. The bottom part of Figure 25 is simply a spectrum of the total energy of the three α-particles.

For all breakups that go through the ^{8}Be ground state we have essentially two two-body decays, also called a sequential decay, and the energy and momentum of the α-particles are determined by conservation laws and thus does not tell us anything about the excited states in ^{12}C. Since we are mainly interested in distinguishing the different contributions to the spectrum we want to use the spin-parity as a handle on the states, and therefore we need a way of determining the spin-parity of the decaying state. As can be seen on Figure 25 there is also some decays that are not on the diagonal, and these decays can not have gone through the ^{8}Be ground state, but must instead be direct breakups or, if one insists on calling it a sequential decay, have gone through the first excited 2^+-state in ^{8}Be. For these breakups there is still information on the spin-parity of the decaying state hidden in the kinematics of the three α-particles and the β-particle, and it is the plan that I should try to extract this information and hopefully help shedding more light on the broad states at low excitation energy in ^{12}C.

7 AUSAlib

In a research group that takes part in many experiments with very different setups it is not possible to have one single analysis software tool to analyse all experiments. This has traditionally meant that each student has spent a lot of time writing his/her own analysis programs or, alternatively, tried learning how to use the programs written by former students, sometimes written in ancient and obscure languages. Even though each analysis is unique, there are many tasks that always need to be done, like conversion of data between different formats, detector calibration, energy loss calculations and simulations, front-back matching of

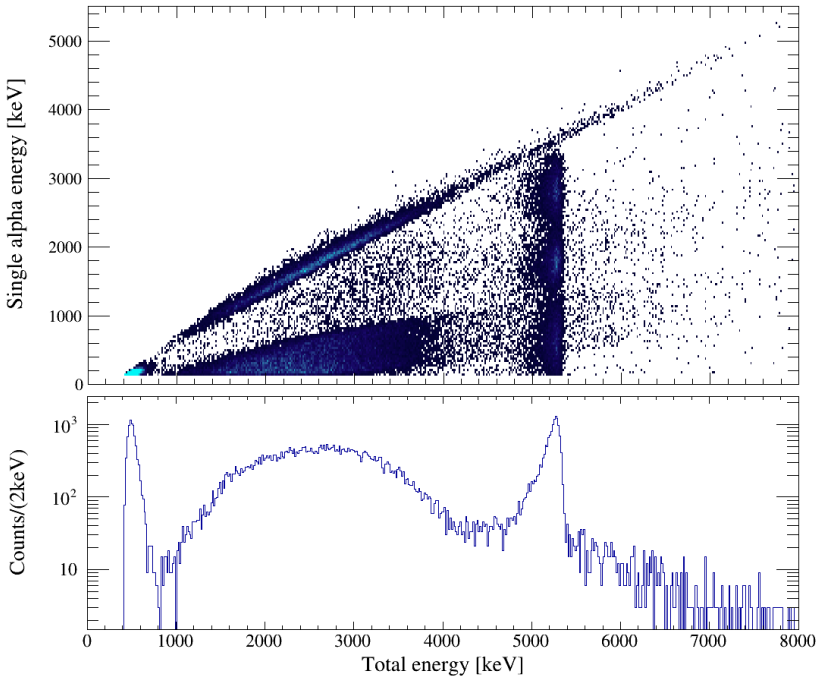

Figure 25: *A plot with approximately two days of beam time worth of data from the JYFL-experiment, containing 25000 events with observed 3α-breakup. In the top is shown the energy of the single α-particles plotted against the total energy of the three detected α-particles, and in the bottom is shown the total energy spectrum.*

DSSSDs and so on. In other words, it should be possible to at least have a kind of software "toolbox" to use for solving these small and trivial tasks, and instead get more time for the more interesting physics analysis. I have spent some effort figuring out ways of creating such a software toolbox, and in the following I describe the basic ideas and principles behind *AUSAlib*[4].

The ROOT analysis framework[29] would be a natural starting point for any modern analysis of data from nuclear or particle physics experiments and, being an object-oriented framework, ROOT is already based on the idea of small classes that are able to solve isolated and general tasks. The first requirement of our toolbox is therefore that it should be easy to integrate with ROOT, and one way of achieving this is to define and implement a collection of classes which are then added to ROOT's dictionary. In that way it should be possible to use the AUSAlib classes in interpreted ROOT scripts, in compiled codes employing the standard ROOT classes and in the interactive ROOT shell. Also I decided to implement my classes as *child classes* of one of the most generic ROOT classes, the `TNamed`-class, and in this way inheriting a lot of functionality, for instance regarding the capability to store the objects in ROOT-files.

The next decision to make is how to organise the toolbox, and how far it is possible to make the analysis generic and experiment-independent. I thought it natural to strictly tie some of the AUSAlib classes to real, physical objects and try to let the capabilities of each class reflect the properties of the physical objects they represent. This has resulted in a collection of "simple" classes, by which I mean classes with very few advanced methods but instead the capability of holding information on the physical objects, an approach which is actually more in line with the old C `struct`. Separate from the `struct`-like classes are the more active "worker"-classes, which do not contain information that needs to be persistent, but instead have the capability to perform advanced tasks. An overview of the entire family is shown in Table 4.

My view of the data flow is sketched in Figure 26, and I believe that all the shown steps can be done by programs that are not specific for the experiment. To do this it is necessary to identify which things are common for all experiments and which are specific. We shall only focus on the things that are common, for instance

[4] AUSA is, if I remember correctly, an acronym for *Aarhus University SubAtomic*.

Table 4: *An overview of the current members of the AUSAlib*

`struct`-*like classes*	*Worker-classes*
`AUSADetector`	`AUSACalibrator`
`AUSADsssd`	`AUSAMatcher`
`AUSASetup`	`AUSABuilder`
`AUSASource`	
`AUSABeam`	
`AUSAEvent`	
`AUSAParticle`	

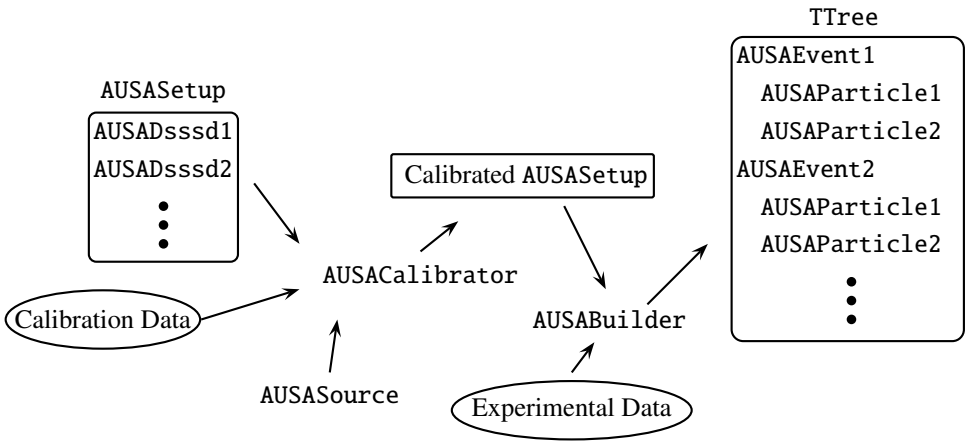

Figure 26: *The data flow of the generic processing. When the setup and source are specified and fed to the calibrator together with the calibration data, the calibrator sorts the data, calculates the calibration parameters and returns the setup with all calibration parameters now stored in the setup object. When the builder is supplied with the calibrated setup and the raw experimental data it performs the event-building, identifying particles and calculating their energy and momentum.*

1. We always have an experimental setup. The setup usually consists of different detectors, DSSSDs, scintillators and so on, placed in a fixed geometry.

2. The detectors are often calibrated with a radioactive source, so we need a class that can search a spectrum for peaks and calculate the calibration parameters.

3. Many times we are interested in the type of detected particle, its energy, its momentum and so on, and not so much in which ADC-channel gave the signal from the particle.

The first point on the list means that we can define a setup-class as a container for detectors, and that we can define a generic detector-class containing information on the position, direction and size of the detector. Sometimes we use more specialised detectors, like DSSSDs, but we can easily implement a DSSSD-class as a child class to the detector-class, and in this way we only need to implement functionality that is specific for the DSSSD. The fact that a DSSSD is just a special kind of detector is thus directly reflected in the class-hierarchy. The second point suggests that there should be a worker-class, a calibrator, that can take a setup-object, a source-object containing information on the peak energies of the used calibration source, and the actual calibration data and return the setup-object in a fully calibrated state. The last point made me think that it would perhaps be convenient to organise the data itself in a more physically motivated structure, and I introduced the event- and particle-classes. The raw data is then interpreted by the event-builder class which converts the ADC-signals to energy and identifies the different particles that were detected in each event. For every physical particle it creates a particle-object and stores it in the event-object, and in the end the result is a ROOT-tree holding all the processed data in these structures.

Storing the data in this way means that the experiment-specific work should be reduced, and that it is not necessary for the physicist to waste a lot of time on "trivial" work like calibration, calculating angles and

momenta and so on. Since the classes are added to ROOT's dictionary it is also possible to use the event- and particle-methods in the `TTree::Draw()`-function in the interactive ROOT-shell, and `AUSAlib` already showed during the JYFL-experiment that it is possible to quickly extract pretty complex information from the data, which is very important during an experiment where you have limited beam time and need to make sure that it is the right beam component that is transmitted to the target chamber, and that it is hitting the target. An interesting future project could be to make Monte Carlo simulation programs that uses the `AUSAlib`-classes, and in that way be able to simulate the behaviour of a setup in a given experiment, including energy losses, coverage etc.

8 Summary

This report describes the work I have done during the first part of my Ph.D. studies. The scrupulous analysis of the KVI-experiment has allowed me to prune the data such that the final value for the branching ratio will be more accurate. Apart from gaining experience from the experimental work I have learned about the most common analysis methods used in nuclear physics and on this basis I have tried to put the analysis work on a general formula, reflected by the class-structure of `AUSAlib`. This object-oriented project has been a good exercise in producing clear and logical software that will hopefully also turn out to be user-friendly enough for other people to use, and I am looking forward to directing more attention to `AUSAlib`. Last but not least the data from the JYFL-experiment looks very promising, and a major part of my remaining Ph.D. studies will be based on this experiment.

Bibliography

[1] C. E. Rolfs and W. S. Rodney, *Cauldrons in the Cosmos* (The University of Chicago Press, 1988).

[2] F. Ajzenberg-Selove, Nuclear Physics A **506**, 1 (1990), ISSN 0375-9474, URL http://www.sciencedirect.com/science/article/pii/037594749090271M.

[3] F. Hoyle, D. Dunbar, W. Wenzel, and W. Whaling, Phys. Rev. **92**, 1095c (1953).

[4] D. N. F. Dunbar, R. E. Pixley, W. A. Wenzel, and W. Whaling, Phys. Rev. **92**, 649 (1953), URL http://link.aps.org/doi/10.1103/PhysRev.92.649.

[5] F. Ajzenberg and T. Lauritsen, Rev. Mod. Phys. **24**, 321 (1952), URL http://link.aps.org/doi/10.1103/RevModPhys.24.321.

[6] H. Kragh, Archive for History of Exact Sciences **64**, 721 (2010), ISSN 0003-9519, URL http://dx.doi.org/10.1007/s00407-010-0068-8.

[7] D. Tilley, H. Weller, and C. Cheves, Nuclear Physics A **564**, 1 (1993), ISSN 0375-9474, URL http://www.sciencedirect.com/science/article/pii/0375947493900737.

[8] H. Morinaga, Phys. Rev. **101**, 254 (1956), URL http://link.aps.org/doi/10.1103/PhysRev.101.254.

[9] C. W. Cook, W. A. Fowler, C. C. Lauritsen, and T. Lauritsen, Phys. Rev. **107**, 508 (1957), URL http://link.aps.org/doi/10.1103/PhysRev.107.508.

[10] C. W. Cook, W. A. Fowler, C. C. Lauritsen, and T. Lauritsen, Phys. Rev. **111**, 567 (1958), URL http://link.aps.org/doi/10.1103/PhysRev.111.567.

[11] H. Morinaga, Physics Letters **21**, 78 (1966), ISSN 0031-9163, URL http://www.sciencedirect.com/science/article/pii/0031916366913497.

[12] F. Barker and P. Treacy, Nuclear Physics **38**, 33 (1962), ISSN 0029-5582, URL http://www.sciencedirect.com/science/article/pii/0029558262910143.

[13] D. H. Wilkinson, D. E. Alburger, A. Gallmann, and P. F. Donovan, Phys. Rev. **130**, 1953 (1963), URL http://link.aps.org/doi/10.1103/PhysRev.130.1953.

[14] R. Bijker and F. Iachello, Phys. Rev. C **61**, 067305 (2000), URL http://link.aps.org/doi/10.1103/PhysRevC.61.067305.

[15] D. J. Marín-Lámbarri, R. Bijker, M. Freer, M. Gai, T. Kokalova, D. J. Parker, and C. Wheldon, Phys. Rev. Lett. **113**, 012502 (2014), URL http://link.aps.org/doi/10.1103/PhysRevLett.113.012502.

[16] S. Hyldegaard, M. Alcorta, B. Bastin, M. J. G. Borge, R. Boutami, S. Brandenburg, J. Büscher, P. Dendooven, C. A. Diget, P. Van Duppen, et al., Phys. Rev. C **81**, 024303 (2010), URL http://link.aps.org/doi/10.1103/PhysRevC.81.024303.

[17] M. Freer, M. Itoh, T. Kawabata, H. Fujita, H. Akimune, Z. Buthelezi, J. Carter, R. W. Fearick, S. V. Förtsch, M. Fujiwara, et al., Phys. Rev. C **86**, 034320 (2012), URL http://link.aps.org/doi/10.1103/PhysRevC.86.034320.

[18] W. R. Zimmerman, M. W. Ahmed, B. Bromberger, S. C. Stave, A. Breskin, V. Dangendorf, T. Delbar, M. Gai, S. S. Henshaw, J. M. Mueller, et al., Phys. Rev. Lett. **110**, 152502 (2013), URL http://link.aps.org/doi/10.1103/PhysRevLett.110.152502.

[19] W. Zimmerman, Ph.D. thesis (2014).

[20] L. Buchmann and C. Barnes, Nuclear Physics A **777**, 254 (2006), ISSN 0375-9474, special Issue on Nuclear Astrophysics, URL http://www.sciencedirect.com/science/article/pii/S0375947405000084.

[21] R. E. Azuma, L. Buchmann, F. C. Barker, C. A. Barnes, J. M. D'Auria, M. Dombsky, U. Giesen, K. P. Jackson, J. D. King, R. G. Korteling, et al., Phys. Rev. C **50**, 1194 (1994), URL http://link.aps.org/doi/10.1103/PhysRevC.50.1194.

[22] L. Buchmann, G. Ruprecht, and C. Ruiz, Phys. Rev. C **80**, 045803 (2009), URL http://link.aps.org/doi/10.1103/PhysRevC.80.045803.

[23] M. Gai, Phys. Rev. C **88**, 062801 (2013), URL http://link.aps.org/doi/10.1103/PhysRevC.88.062801.

[24] K. Neubeck, H. Schober, and H. Wäffler, Phys. Rev. C **10**, 320 (1974), URL http://link.aps.org/doi/10.1103/PhysRevC.10.320.

[25] G. Berg, O. Dermois, U. Dammalapati, P. Dendooven, M. Harakeh, K. Jungmann, C. Onderwater, A. Rogachevskiy, M. Sohani, E. Traykov, et al., Nuclear Instruments and Methods in Physics Research Section A: Accelerators, Spectrometers, Detectors and Associated Equipment **560**, 169 (2006), ISSN 0168-9002, URL http://www.sciencedirect.com/science/article/pii/S0168900205026276.

[26] P. Sellin, P. Woods, D. Branford, T. Davinson, N. Davis, D. Ireland, K. Livingston, R. Page, A. Shotter, S. Hofmann, et al., Nuclear Instruments and Methods in Physics Research Section A: Accelerators, Spectrometers, Detectors and Associated Equipment **311**, 217 (1992), ISSN 0168-9002, URL http://www.sciencedirect.com/science/article/pii/0168900292908674.

[27] L. Hubbeling, M. Turala, P. Weilhammer, R. Brenner, I. Hietanen, J. Lindgren, T. Tuuva, W. Dulinski, D. Husson, A. Lounis, et al., Nuclear Instruments and Methods in Physics Research Section A: Accelerators, Spectrometers, Detectors and Associated Equipment **310**, 197 (1991), ISSN 0168-9002, URL http://www.sciencedirect.com/science/article/pii/016890029191025Q.

[28] A. Rytz, Atomic Data and Nuclear Data Tables **47**, 205 (1991), ISSN 0092-640X, URL http://www.sciencedirect.com/science/article/pii/0092640X9190002L.

[29] *Root data analysis framework*, CERN webpage, URL http://root.cern.ch/drupal/.

[30] *Astar: Stopping power and range tables for alpha particles*, NIST webpage, URL http://physics.nist.gov/PhysRefData/Star/Text/ASTAR.html.

[31] O. Kirsebom, H. Fynbo, K. Riisager, R. Raabe, and T. Roger, Nuclear Instruments and Methods in Physics Research Section A: Accelerators, Spectrometers, Detectors and Associated Equipment **758**, 57 (2014), ISSN 0168-9002, URL http://www.sciencedirect.com/science/article/pii/S016890021400504X.

[32] D. Tilley, C. Cheves, J. Kelley, S. Raman, and H. Weller, Nuclear Physics A **636**, 249 (1998), ISSN 0375-9474, URL http://www.sciencedirect.com/science/article/pii/S0375947498001298.

[33] J. W. Müller, Nuclear Instruments and Methods in Physics Research Section A: Accelerators, Spectrometers, Detectors and Associated Equipment **301**, 543 (1991), ISSN 0168-9002, URL http://www.sciencedirect.com/science/article/pii/016890029190021H.

[34] J. Yorkston, A. Shotter, D. Syme, and G. Huxtable, Nuclear Instruments and Methods in Physics Research Section A: Accelerators, Spectrometers, Detectors and Associated Equipment **262**, 353 (1987), ISSN 0168-9002, URL http://www.sciencedirect.com/science/article/pii/0168900287908734.

[35] H. O. U. Fynbo, Y. Prezado, U. C. Bergmann, M. J. G. Borge, P. Dendooven, W. X. Huang, J. Huikari, H. Jeppesen, P. Jones, B. Jonson, et al., Phys. Rev. Lett. **91**, 082502 (2003), URL http://link.aps.org/doi/10.1103/PhysRevLett.91.082502.

[36] H. O. U. Fynbo, C. A. Diget, U. C. Bergmann, M. J. G. Borge, J. Cederkall, P. Dendooven, L. M. Fraile, S. Franchoo, V. N. Fedosseev, B. R. Fulton, et al., Nature **433**, 136 (2005), URL http://dx.doi.org/10.1038/nature03219.

[37] I. Moore, T. Eronen, D. Gorelov, J. Hakala, A. Jokinen, A. Kankainen, V. Kolhinen, J. Koponen, H. Penttilä, I. Pohjalainen, et al., Nuclear Instruments and Methods in Physics Research Section B: Beam Interactions with Materials and Atoms **317, Part B**, 208 (2013), ISSN 0168-583X, {XVIth} International Conference on ElectroMagnetic Isotope Separators and Techniques Related to their Applications, December 2–7, 2012 at Matsue, Japan, URL http://www.sciencedirect.com/science/article/pii/S0168583X13007143.

[38] P. Dendooven, Nuclear Instruments and Methods in Physics Research Section B: Beam Interactions with Materials and Atoms **126**, 182 (1997), ISSN 0168-583X, international Conference on Electromagnetic Isotope Separators and Techniques Related to Their Applications, URL http://www.sciencedirect.com/science/article/pii/S0168583X96010105.